nature communications

Article

https://doi.org/10.1038/s41467-024-55084-2

Alcohol-induced gut microbial reorganization and associated overproduction of phenylacetylglutamine promotes cardiovascular disease

Received: 24 April 2024

Accepted: 27 November 2024

Published online: 30 December 2024

Check for updates

Zhen Li[1], Min Gu[2,19], Aline Zaparte[2,3], Xiaoming Fu[4,5], Kala Mahen[4,5,6,7], Marko Mrdjen[4,5,6,7], Xinmin S. Li[4,5], Zhihong Yang[8], Jing Ma[8], Themis Thoudam[8], Kristina Chandler[8], Maggie Hesler[8], Laura Heathers[9], Kiersten Gorse[10], Thanh Trung Van[10], David Wong[11], Aaron M. Gibson[12], Zeneng Wang[4,6], Christopher M. Taylor[3,13], Pearl Quijada[11], Catherine A. Makarewich[12,14], Stanley L. Hazen[4,5,15], Suthat Liangpunsakul[8,16,17], J. Mark Brown[4,5,6,7], David J. Lefer[1], David A. Welsh[2,3] & Thomas E. Sharp III[10,18]

The mechanism(s) underlying gut microbial metabolite (GMM) contribution towards alcohol-mediated cardiovascular disease (CVD) is unknown. Herein we observe elevation in circulating phenylacetylglutamine (PAGln), a known CVD-associated GMM, in individuals living with alcohol use disorder. In a male murine binge-on-chronic alcohol model, we confirm gut microbial reorganization, elevation in PAGln levels, and the presence of cardiovascular pathophysiology. Fecal microbiota transplantation from pair-/alcohol-fed mice into naïve male mice demonstrates the transmissibility of PAGln production and the CVD phenotype. Independent of alcohol exposure, pharmacological-mediated increases in PAGln elicits direct cardiac and vascular dysfunction. PAGln induced hypercontractility and altered calcium cycling in isolated cardiomyocytes providing evidence of improper relaxation which corresponds to elevated filling pressures observed in vivo. Furthermore, PAGln directly induces vascular endothelial cell activation through induction of oxidative stress leading to endothelial cell dysfunction. We thus reveal that the alcohol-induced microbial reorganization and resultant GMM elevation, specifically PAGln, directly contributes to CVD.

Cardiovascular disease (CVD) remains the leading cause of morbidity and death worldwide. Despite improved management of contemporary CVD comorbidities, the contribution of modifiable risk factors, such as alcohol consumption, has been continually debated[1]. A recent genome-wide association study demonstrated that the presumed benefits of alcohol consumption were instead attributable to favorable lifestyle factors not taken into consideration in many prior clinical studies[2]. The data revealed that independent of the weekly amount consumed, alcohol positively correlated with CVD incidence. An earlier report indicated hazardous alcohol use predicts future manifestation of cardiovascular-related disorders[3]. The murine binge-on-chronic alcohol (BoCA)

A full list of affiliations appears at the end of the paper. e-mail: tesharp@usf.edu

and other models of alcohol use disorders have linked alcohol to increased oxidative stress, mitochondrial dysfunction, and inflammation—all of which are well-recognized contributors to CVDs[4]. However, these direct cellular consequences of alcohol fail to account for the total increased risk of cardiovascular morbidity in those who consume alcohol in excess.

Alcohol-related organ damage has been classically associated with liver diseases[5] along with disruption to gut homeostasis, including microbial reorganization and increased gut permeability[6]. The gut microbiome produces a plethora of signaling metabolites that alter host cellular homeostasis and organ function. This is best exemplified by gut-microbial production of trimethylamine and subsequent oxidation by flavin-monooxygenases in the liver to produce trimethylamine *N*-oxide (TMAO). TMAO has been well-established to mediate pathological signaling within the host including association with alcohol misuse[7,8]. Metabolism of aromatic amino acid phenylalanine, produces gut microbial metabolites (GMM) which have recently garnered emerging interest in numerous disease states[9]. The phenylalanine metabolite alpha-*N*-phenylacetyl-*L*-glutamine (phenylacetylglutamine [PAGln]), is a GMM classified as a uremic toxin associated with cardiovascular (CV) and renal diseases[10]. PAGln was identified through untargeted metabolomic analysis in a large-scale clinical study to be increased in circulation and associated with CV-related disease and major adverse cardiovascular events (i.e., stroke, myocardial infarction, and death)[11]. Subsequent mechanistic studies elucidated PAGln's capacity to signal through adrenergic receptors on platelets and increasing the likelihood of thrombi formation[11]. Most recently, PAGln levels were positively associated with heart failure, independent of ejection fraction, and shown to have mechanistic links to relevant CV phenotypes in several studies[12].

There is a paucity of data regarding hazardous alcohol use and the gut-CV relationship. We reasoned that alcohol-dependent dysregulation of gut homeostasis would lead to an increased abundance of pathogenic GMMs, promoting increased susceptibility to cardiovascular dysfunction in the host. Herein, we employ multiple murine models to corroborate alcohol's effects on gut homeostasis and host physiology. We further designed experiments to establish that alcohol-induced microbial reorganization, independent of other co-factors, was sufficient to elevate levels of deleterious GMMs, which in-part promotes cardiac and vascular pathophysiology. Coupled with in vitro studies, we demonstrate the direct effects of PAGln as a driver of aberrant cardiomyocyte contractility, vascular endothelial activation, and contributor towards the pathogenesis of CVD.

Results

PAGln is elevated in patients with alcohol use disorder

In a cohort of individuals who were determined to be heavy drinkers (HD) based upon their Alcohol Use Disorder Identification Test Corrected (AUDIT-C) score, we analyzed serum samples using LC-MS/MS for semi-quantitative levels of circulating metabolites as previously described[13]. Of those targets that were identified, PAGln was observed to be significantly elevated ($p = 0.009$) in the HD ($n = 126$) in comparison to healthy controls (HC) ($n = 22$) (Fig. 1A). The serum PAGln levels of HDs were significantly ($p = 0.023$) associated with increased AUDIT-C scores at the time of admission (Fig. 1B) demonstrating a positive correlation between alcohol use and circulating PAGln levels. Within the cohort we investigated sexual dimorphism amongst HDs and PAGln levels in comparison to HCs. HD men had significantly higher PAGln levels than their respective control counterparts (Fig. 1C). In contrast, woman HDs did not statistically differ from HC women (Fig. 1D). This sexual dimorphism within this cohort led us to investigate the mechanism(s) by which alcohol could lead to elevation in GMM PAGln and the physiological effects on the host cardiovascular system in male murine models.

Alcohol-related organ damage and cardiovascular dysfunction

In an initial study, we wanted to recapitulate the previously reported adverse cardiovascular effects of binge-on-chronic alcohol (BoCA)[14] (Fig. 2A) while determining any beneficial effect of modulating the gut meta-organismal milieu with probiotic supplementation given the previous observation of alcohol-induced gut microbial reorganization[15]. In the presence of hazardous alcohol use, probiotic microbes (in isolation or combination) including those combined in this study (*Lactobacillus plantarum, Lactobacillus rhamnosus, Lactobacillus reuteri 1E, Bifidobacterium bifidum*, and *Bifidobacterium animalis*; [L3B2]), have shown in preclinical models and in humans to alter microbiome structure and function by restoring normal bowel flora, and improving intestinal barrier, and subsequent host end organ damage[16]. Herein, mice were randomized to three groups: (1) pair-fed (PF) controls, (2) binge-on-chronic ethanol (alcohol-fed [AF]), or (3) alcohol-fed + probiotics L3B2 (AF + P). Mortality was similar across groups at 20-days (Supplementary Fig. 1a) and no difference in body weight (Supplementary Fig. 1b), indicating similar caloric intake in all mice. In a subset analysis, 2 h post-binge blood alcohol levels were elevated (Supplementary Fig. 1c), confirming binge exposure in the AF ± P mice. In measuring circulating antioxidant capacity through 8-isoprostane levels, we observed no difference between PF and AF, yet a significant reduction in AF + P cohort (Supplementary Fig. 1d) suggestive of increased antioxidant capability in those mice.

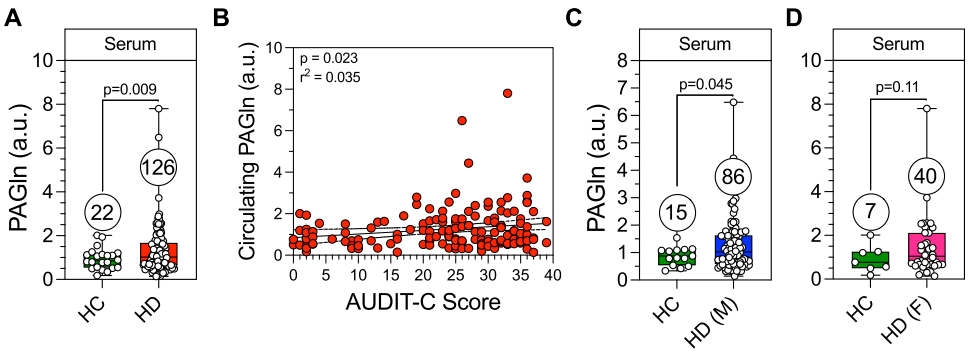

Fig. 1 | PAGln levels in patients with alcohol use disorder. A Healthy controls (HC, green) and heavy drinkers (HD, red) serum levels of phenylacetylglutamine (PAGln). **B** Association between PAGln levels and self-reported AUDIT-C scores upon admission. Linear regression analysis was performed demonstrating the line of best-fit with the 95% confidence interval. **C**, **D** Serum PAGln levels in male (blue) and female (pink) HC (green) and HD, respectively. All data (**A**, **C** and **D**) are presented as box and whisker plots (mean, max, and min.) with individual measurement dot plots unless otherwise stated. Number of patients enrolled in each measurement is found in open circle. Significance ($p < 0.05$) was determined by Kruskal-Wallis Test with Dunn's multiple comparisons test (two-sided) unless stated otherwise.

https://doi.org/10.1038/s41467-024-55084-2

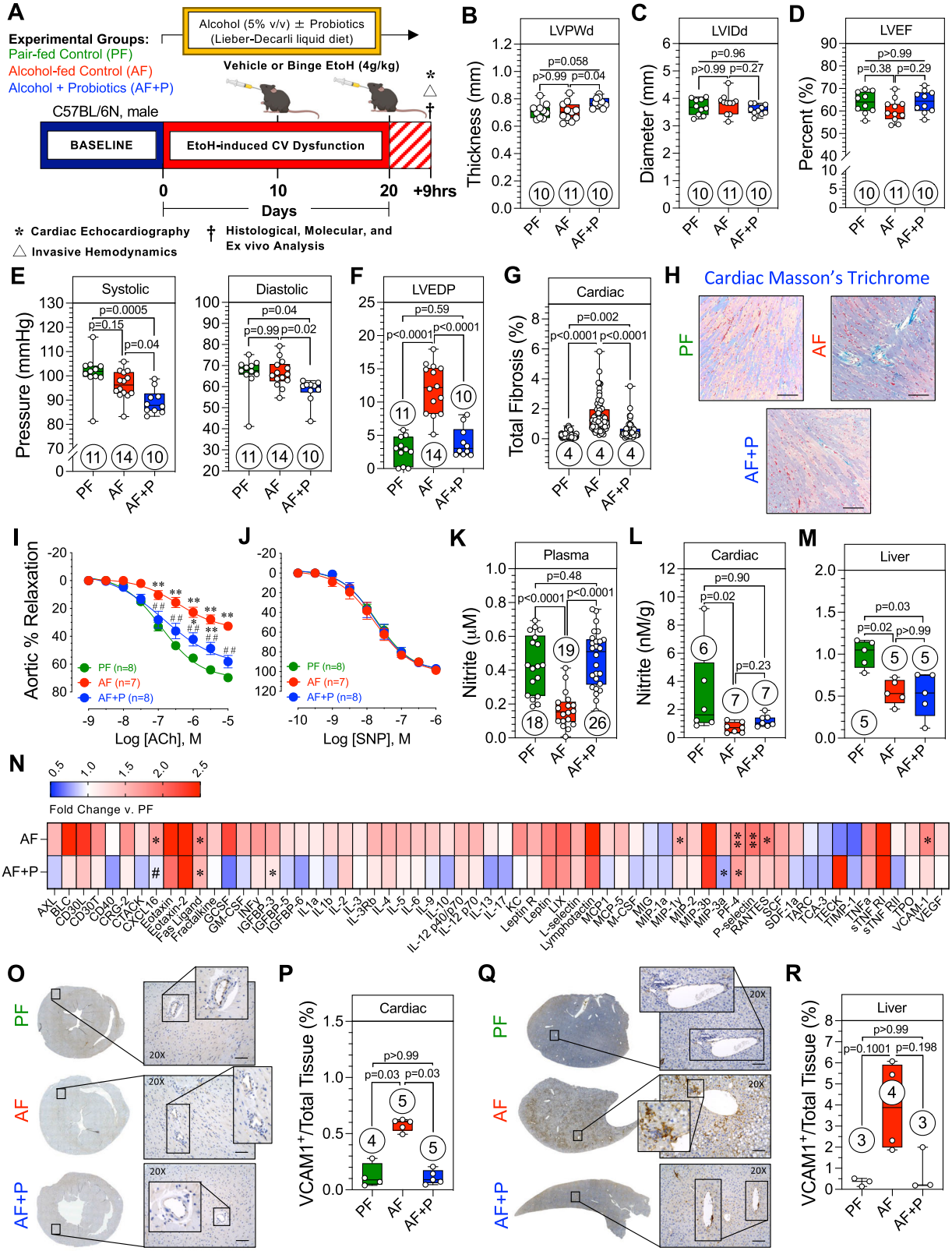

Alcohol-related liver disease is the hallmark of hazardous alcohol use. Liver/body weight ratio (Supplementary Fig. 1e) was increased in the AF group compared to PF and AF + P groups while key markers of liver damage were elevated in the 20-day exposure period (Supplementary Fig. 1f, g). To identify the hepatic inflammatory response, transcriptional expression of pro- and anti-inflammatory markers were measured (Supplementary Fig. 1h–k). Tumor necrosis factor-alpha was increased in the livers of AF mice, while expression of the anti-inflammatory cytokine interleukin-10 was increased in the livers of AF + P mice, confirming the anti-inflammatory properties of L3B2 administration[17]. Histological assessment revealed alcoholic liver steatosis and fibrosis were confirmed in the AF cohort where there was an increased steatosis score and fibrosis percentage compared to both PF and AF + P (Supplementary Fig. 1l–n). Taken together, these data

Fig. 2 | Alcohol-related organ damage and cardiovascular dysfunction. **A** Experimental protocol of murine 20-day binge-on-chronic alcohol (BoCA) model. Three treatment cohorts were enrolled: pair-fed (PF, green); alcohol-fed (AF, red); alcohol-fed + probiotics L3B2 (AF + P, blue). Created in BioRender. Sharp, T. (2024) https://BioRender.com/x77k051. **B**–**D** Echocardiographic measurements of structure and function. LVPWd left ventricular posterior wall-diastole. LVIDd left ventricular internal diameter-diastole. LVEF left ventricular ejection fraction from a single cohort of mice. **E** Systemic invasive hemodynamics, systolic and diastolic blood pressure from two separate experiments. **F** Left ventricular end-diastolic pressure from two separate experiments. **G** Quantification of Masson's Trichrome stain as a percentage of total tissue area from a single experiment. Statistical analysis was determined by repeated measures two-way ANOVA with a Bonferroni's multiple comparisons test (two-sided). **H** Representative 20× magnification brightfield microscopy of Masson's Trichrome staining (blue) of myocardium. Scale bar = 100 µm. **I**, **J** Aortic vasorelaxation to acetylcholine (ACh) and sodium nitroprusside (SNP). Statistical analysis was determined by repeated measures two-way ANOVA with a Bonferroni's multiple comparisons test (two-sided). (*) p-value < 0.05 PF vs. AF + P [blue line]; (**) p-value < 0.0001 PF vs. AF [red line], PF vs. AF + P [blue line]; ($^{\#\#}$) p-value < 0.01 AF + P vs. AF [blue line]. Non-linear fit lines for each treatment were plotted using log(agonist) vs response four-parameter variable slope. **K**–**M** Plasma (from multiple studies), cardiac, and liver (from a single study) nitrite levels. **N** Plasma cytokine levels as fold change compared to pair-fed. Statistical significance determined by two-way ANOVA with Geisser-Greenhouse correction with Tukey's multiple comparison test. $N = 7$ per group. **O** Representative microscopy of cardiac vascular cell adhesion molecule (VCAM-1, brown) at 20× magnification. Scale bar = 50 µm. Magnification of the vessel. **P** Quantification of cardiac VCAM-1 positive blood vessels as percentage of total tissue area. **Q** Representative microscopy of liver VCAM-1 at 20× magnification. Scale bar = 50 µm. Magnification of vessel. **R** Quantification of liver VCAM-1 positive blood vessels as percentage of total tissue area. All data (2B-G, 2K-M, 2P and 2R) are presented as box and whisker plots (mean, max, and min.) with individual measurement dot plots unless otherwise stated. Number of mice enrolled in each measurement is found in open circle. Significance ($p < 0.05$) was determined by Kruskal-Wallis Test with Dunn's multiple comparisons test (two-sided) unless stated otherwise.

confirm animals enrolled in AF group exhibited classical alcohol-related liver pathology and L3B2-induced gut microbial modulation alleviated such end-organ damage.

We also examined measures of cardiac structure and function through transthoracic echocardiography and invasive hemodynamics. A lack of cardiac remodeling (as measured by posterior wall thickness [LVPWd] [hypertrophic remodeling] or internal dimension [LVIDd] [LV dilation]) and no change in left ventricular ejection fraction (LVEF) (Fig. 2B–D, Supplementary Table 1) is consistent with patients who abuse alcohol and whose cardiac dimensions are relatively unchanged despite disease manifestation during the asymptomatic phase[18]. In assessing systemic and central hemodynamics, proximal aortic arterial pressures were unchanged (Fig. 2E), however, the blood pressure lowering effect of probiotics administration, in general, was observed as previously described in patients[19]. Left ventricular end-diastolic filling pressure (LVEDP) in AF mice (Fig. 2F) was elevated with no difference in the relaxation time constant, Tau (Supplementary Fig. 1o). This marked elevation in LVEDP suggests central congestion, irrespective of no change in afterload (systemic pressure), and is a hallmark of heart failure[20]. Left ventricular systolic pressure remained unchanged across all groups (Supplementary Fig. 1p). AF + P animals had a substantial reduction in LVEDP in comparison to their AF counterparts (Fig. 2F). Given the aberrant diastolic hemodynamics, we assessed cardiac fibrosis as a contributor towards myocardial stiffening. There was an increase in cardiac fibrosis in the AF cohort compared to other groups (Fig. 2G, H); however, it is likely a marginal contributor to myocardial stiffness compared to the drastic changes observed in LV filling pressures in AF mice. Interestingly, these results suggest that in the absence of adverse cardiac remodeling and systolic dysfunction by echocardiography, there are still ventricular hemodynamic abnormalities consistent with an altered ability of myocardium to relax properly during diastole, despite no change in afterload, indicating a direct effect on the myocardium.

To determine the effects of alcohol on the vasodilatory properties of the arterial vasculature we performed ex vivo vascular reactivity assays as previously described[21]. Animals subjected to BoCA had a profound reduction in their ability to relax in response to acetylcholine. Maximal relaxation to acetylcholine was reduced by 47% in the AF versus PF group. In addition, the lack of difference in response to sodium nitroprusside, a nitric oxide donor and endothelial-independent vasodilator, led us to conclude BoCA induces endothelial dysfunction. In contrast, supplementation with L3B2 protected against the deleterious effects of alcohol exposure (Fig. 2I, J and Supplementary Fig. 1q, r). To further assess vascular endothelial health, plasma nitrite was measured by high-performance liquid chromatography as a biomarker of bioavailable nitric oxide. This nitrite pool has been identified as a marker of endothelial health and is reduced in numerous cardiovascular-related diseases[22]. Notably, those mice subjected to BoCA had a 38% reduction in plasma nitrite (Fig. 2K). Concomitant administration of L3B2 significantly inhibited the reduction in plasma nitrite, preserving normal physiological levels compared to AF-treated mice. We then investigated cardiac and liver nitrite levels (Fig. 2L, M) and found that there were reductions in both cardiac and liver nitrite in the AF compared to the PF group. However, L3B2 supplementation did not seem to attenuate the deficit. To determine the circulating cytokine milieu and vascular endothelial activation we next performed an array analysis of anti- and pro-inflammatory cytokines in plasma samples from all groups (Fig. 2N and Supplementary Fig. 1s). Overall, the AF animals had an increased proinflammatory cytokine profile as compared to the PF mice. Vascular endothelial activation was confirmed by an increased abundance of circulating P-selectin and vascular endothelial adhesion molecule 1 (VCAM-1) in the AF group. This was inhibited by L3B2, further demonstrating therapeutic potential of altering the gut microbial environment (Fig. 2N). The platelet aggregation promoting cytokine, platelet factor 4 (PF-4), was upregulated in the AF compared to PF animals, which in turn was attenuated with L3B2 supplementation. Given the changes in vascular adhesion molecules, immunohistochemistry was performed and analyzed for cardiac and hepatic endothelial VCAM-1 expression. VCAM-1 was increased in AF mice compared to the PF corroborating the vascular endothelial dysfunction and circulating cytokine profile (Fig. 2O–R).

In totality, alcohol leads to central effects on LV diastolic hemodynamics, vascular endothelial dysfunction and activation, and a proinflammatory milieu. Further, it has been recently established that alcohol consumption leads to gut microbial reorganization which plays a critical role in maintenance of normal host physiology[23]. Through these initial studies, the benefits afforded by the use of a concomitant L3B2 in AF mice indicate the gut microbiome may play a critical role in alcohol-related organ damage. We next sought to investigate gut microbial composition, through metagenomic analysis, and intestinal homeostasis in these three groups.

Alcohol disrupts gut homeostasis through microbial reorganization, gut leak, and altered immunity

Gut microbial 16S rRNA gene sequencing was performed on the cecal content of a subset of animals. Microbial community heterogeneity was assessed through population analysis of α- and β-diversity (Fig. 3A, B). There was a marked reduction in α-diversity (Observed and ACE) within AF compared to PF mice confirming gut microbial community reorganization[24]. The microbial phylogenetic distance was assessed through unique fraction metric (i.e., unifrac) between the three cohorts and confirmed shifts within microbial populations (Fig. 3B). The *Firmicutes* to *Bacteroidetes* ratio, a hallmark of dysbiosis,

https://doi.org/10.1038/s41467-024-55084-2

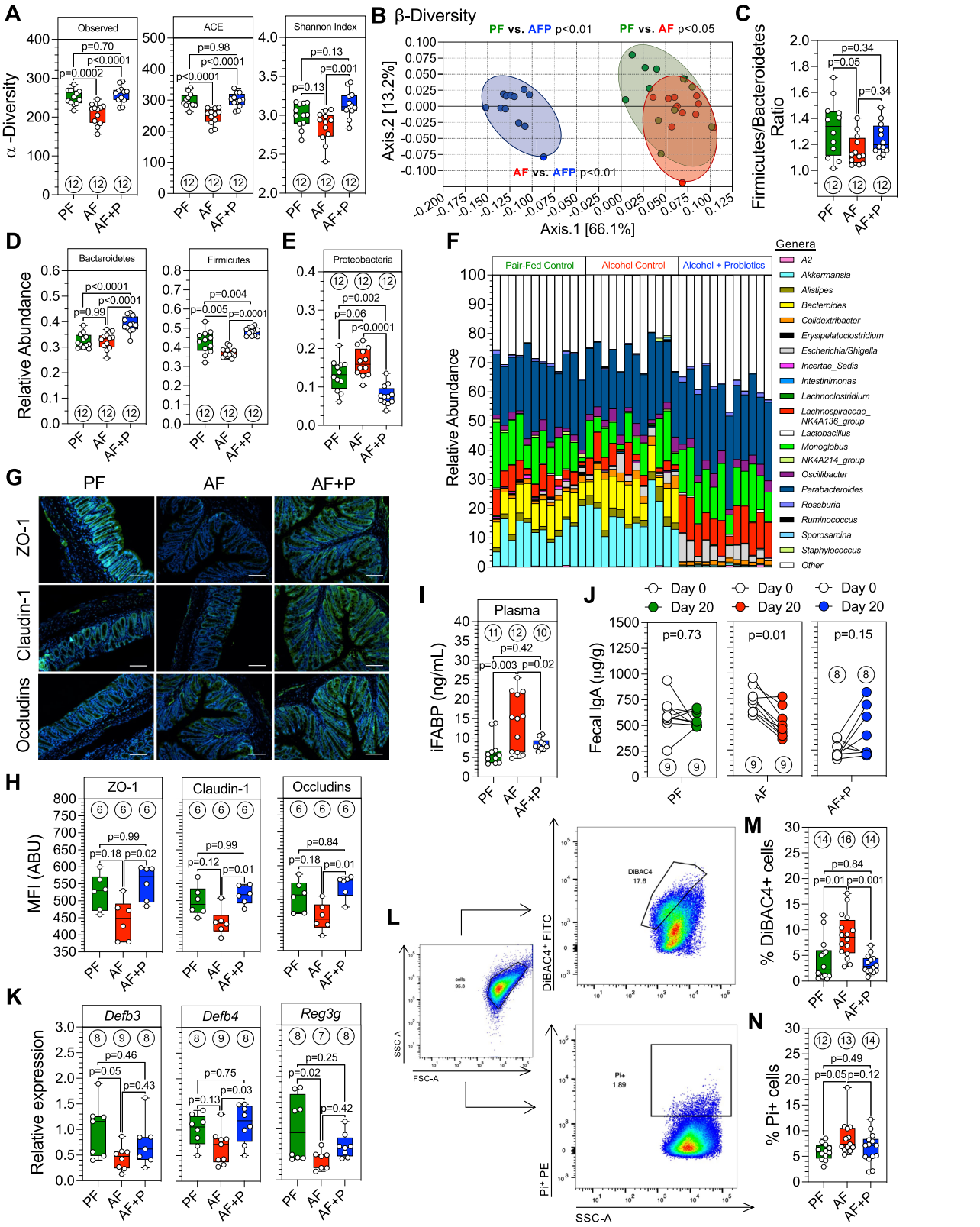

was significantly reduced in AF mice compared to PF counterparts (Fig. 3C). The relative abundance of these two major phyla demonstrated little to no change in *Bacteriodetes* in the AF cohort. In contrast, the relative abundance of *Firmicutes*, was decreased within the BoCA cohort and protected in the AF + P cohort (Fig. 3D). In addition, low abundance of *Firmicutes* has been linked to several disease states[25], *Proteobacteria*, a phyla associated with intestinal and extra-intestinal diseases[26], was elevated in relative abundance in AF mice (Fig. 3E). In Fig. 3E, L3B2 reversed this *Proteobacteria* elevation, demonstrating a compositional change in the gut microbiome of the AF + P group. Further analysis of the metagenomic data demonstrated overall changes in the genera between all three groups, plotted in Fig. 3F are the top 20 genera altered between PF and AF cohorts, which confirms the micro-organismal reorganization induced by alcohol. The use of probiotics further confirms that reorganization of the microbiome, despite not returning to a similar composition of PF, is critical to the

Fig. 3 | Alcohol consumption disrupts gut homeostasis through microbial community reorganization, gut leak, and altered gut immunity. A Alpha diversity—observed, ACE, and Shannon Index. **B** Beta diversity—unweighted unique fraction metric (UniFrac) beta-diversity of PF, AF, and AF + P. Dots represent individual samples. Statistical analysis was determined using PERMANOVA. **C** *Firmicutes*/*Bacteriodetes* ratio. **D** Individual relative abundance of *Firmicutes* and *Bacteriodetes*. **E** Relative abundance of *Proteobacteria*. **F** Bar graph of top 20 genera relative abundance altered between PF, AF, and AF + P. **G**, **H** Representative fluorescent images at 20× magnification of tight junction protein 1 (ZO-1), Claudin-1, and Occludins (green). DAPI nuclear stain (blue). Scale bar = 100 µM. Quantification of mean fluorescent intensity of each target per group. **i** Plasma levels of intestinal fatty-acid binding protein (iFABP). **J** Fecal immunoglobulin A (IgA) levels. Data presented as independent biological replicates. Number of mice enrolled in each measurement is found in open circle. Statistical significance ($p < 0.05$) was determined by paired Student's *T*-test (two-tailed) between baseline and day 20. Dot plots represent individual measurements. **K** Relative mRNA expression of βDefensin-3, βDefensin-4, and Reg-3r in fecal samples at day 20. **I** Representative flow cytometric gating for analysis of bacterial cell damage and death. **M** Bis-(1,3-Dibutylbarbituric Acid) Trimethine Oxonol (DiBAC4) positive bacterial cell quantification per group as a percentage of total cells. **N** Propidium Iodide (Pi) positive bacterial cell quantification per group as a percentage of total cells. All data (**A**, **C**–**E**, **H**, **I**, **K**–**N**) are presented as box and whisker plots (mean, max, and min.) with individual measurement dot plots unless stated otherwise from a single experiment. Pair-fed (PF, green); alcohol-fed (AF, red); alcohol-fed + probiotics L3B2 (AF + P, blue) unless otherwise stated. Number of mice enrolled in each measurement is found in open circle. Significance ($p < 0.05$) was determined by one-way ANOVA with Holm-Šídák multiple comparisons test (two-sided) unless stated otherwise.

protection of the gut in the presence of alcohol (Fig. 3F). We quantified the relative abundance of each of the microbes in L3B2 (*Lactobacillus plantarum, Lactobacillus rhamnosus, Lactobacillus reuteri 1E, Bifidobacterium bifidum*, and *Bifidobacterium animalis*) in cecal samples (Supplementary Fig. 2a–e). Compared to the AF counterparts each microbe was significantly elevated in the AF + P group.

Increased gut permeability is a major consequence of continual excessive alcohol consumption[27] and a driver in the pathogenesis of a myriad of disorders[28]. Dynamic regulatory proteins are critical to the maintenance of the intestinal barrier between the gut lumen and host[29]. Zonula occludens-1, claudin-1, and occludin are essential inter- and intracellular structural proteins that help regulate the movement of water, solutes and immune cells across the intestinal barrier. In immunohistochemistry studies (Fig. 3G, H) these three essential gut permeability proteins were all reduced in the AF compared to PF cohort. L3B2 supplementation inhibited the deleterious effects of alcohol consumption on gut permeability (Fig. 3H). Circulating levels of intestinal fatty-acid binding protein, which should be undetectable in the plasma under healthy conditions, were significantly elevated with alcohol exposure; this gut leak was inhibited with concomitant L3B2 (Fig. 3I). Dietary alterations profoundly affect the critical interplay between the gut microbiome and host's innate immune system, which have evolved to co-exist over millennia[30]. Immunoglobulin-A levels and expression of antimicrobial peptides are gastrointestinal markers that provide insight into gut immunity and potential etiology of gut-centric disease processes[31]. Expression of antimicrobial peptides are a first line of defense in the gut's innate immune system. Defensins are a large family of cationic antimicrobial peptides produced by the epithelial cells of the gut lining that inhibit bacterial growth through membrane disruption and cell wall synthesis[32]. Herein we observed a reduction in fecal immunoglobulin-A (Fig. 3J) and expression of antimicrobial peptides (Fig. 3K) in the BoCA-fed mice compared to baseline or treatment group respectively, indicating compromised gut immunity. Thus, these studies demonstrate that BoCA consumption, independent of other dietary modifications, promotes microbial community restructuring and leads to a reduction in the necessary innate immune characteristics of the gut for proper physiological intestinal homeostasis.

Due to microbial reorganization, gut leak, and altered immune profile, we analyzed gut flora damage and death using single-cell flow cytometry fluorometric quantification as previously described[33]. Representative gating demonstrates the shift in the populations corresponding to fecal bacterial cell damage or death (Fig. 3L). Bis-(1,3-Dibutylbarbituric Acid)-trimethine oxonol (DiBAC4) is a voltage-sensitive fluorescent probe which when taken up by a cell indicates membrane damage. In the AF mice, $DiBAC4^+$ bacteria increased in comparison to PF and AF + P (Fig. 3M). Bacterial cell death was measured through incubation with propidium iodide (Pi) which cannot be taken up by viable bacteria. As a percentage of the total bacteria count, we observed an increase in PI^+ cells with BoCA-feeding (Fig. 3N).

Collectively, these experiments demonstrate a clear influence of chronic and excessive alcohol consumption on gut bacteria viability, independent of other dietary alterations, through induction of gut microbial reorganization, increased paracellular permeability, augmented intestinal innate immunity, and direct microbial cytotoxicity. Given that the gut-host interaction is necessary for the maintenance of normal host physiological functions and the considerable evidence implying its' role in the pathogenesis of a myriad of diseases including CVD[9], we sought to provide a mechanism by which dysregulated gut homeostasis due to BoCA consumption could drive cardiovascular dysfunction.

Elevated PAGln is associated with cardiovacular pathophysiology

To understand the link between alcohol-induced gut microbial reorganization, intestinal dysregulation, and host physiological responses we performed targeted gut-microbial-derived metabolite profiling on plasma and tissues samples collected from animals. In the BoCA study, we focused on select GMMs and their precursors which are known mediators of host CV pathophysiology[34]. Previous work by Nemet et al.[9] began with nearly 100 candidate gut microbiome-related aromatic amino acid-derived metabolites and narrowed the panel to the 2–3 dozen select metabolites due to their associations with incident MACE or alternative metabolic phenotypes, as well as detection in the majority (>75%) of plasma samples of subjects. We hypothesized that the difference in CVD phenotypes elicited by AF ± P might be mediated in part by this subset of gut microbiota-derived products, we performed targeted LC-MS/MS analyses with this panel and identified a notable signal in the circulating levels of PAGln among mice exposed to alcohol. PAGln, a gut microbiota-derived phenylalanine metabolite, is one of the selected metabolites which is elevated in cardiometabolic disease, including chronic kidney disease and heart failure[10]. Briefly, phenylalanine is converted through aminotransferases to phenylpyruvic acid in the gut. Two distinct pathways lead to microbial conversion of phenylpyruvic acid to phenylacetic acid (PAA)[35]. PAA gives rise to the acetyl-CoA intermediate which combines with either glycine (phenylacetylglycine [PAGly]) or glutamine (PAGln) through their respective transferases. A schematic of the gut microbial and host-dependent processes is illustrated in Fig. 4A. Using tandem mass spectrometry as previously described[11], we measured plasma levels of PAA, PAGly, and PAGln. PAA plasma levels were unchanged irrespective of BoCA or L3B2 supplementation (Fig. 4B). Previous reports have found that rodents predominately produce the PAGly variant, while PAGln is produced in *Homo sapiens*[11]. Interestingly, we observed no significant change in PAGly (Fig. 4C), yet observed increased PAGln levels in plasma samples from BoCA-fed mice compared to PF animals, which was almost undetectable (Fig. 4D). This was significantly attenuated in the presence of L3B2 by more than 50% as compared to the AF cohort. The plasma and tissue levels

https://doi.org/10.1038/s41467-024-55084-2

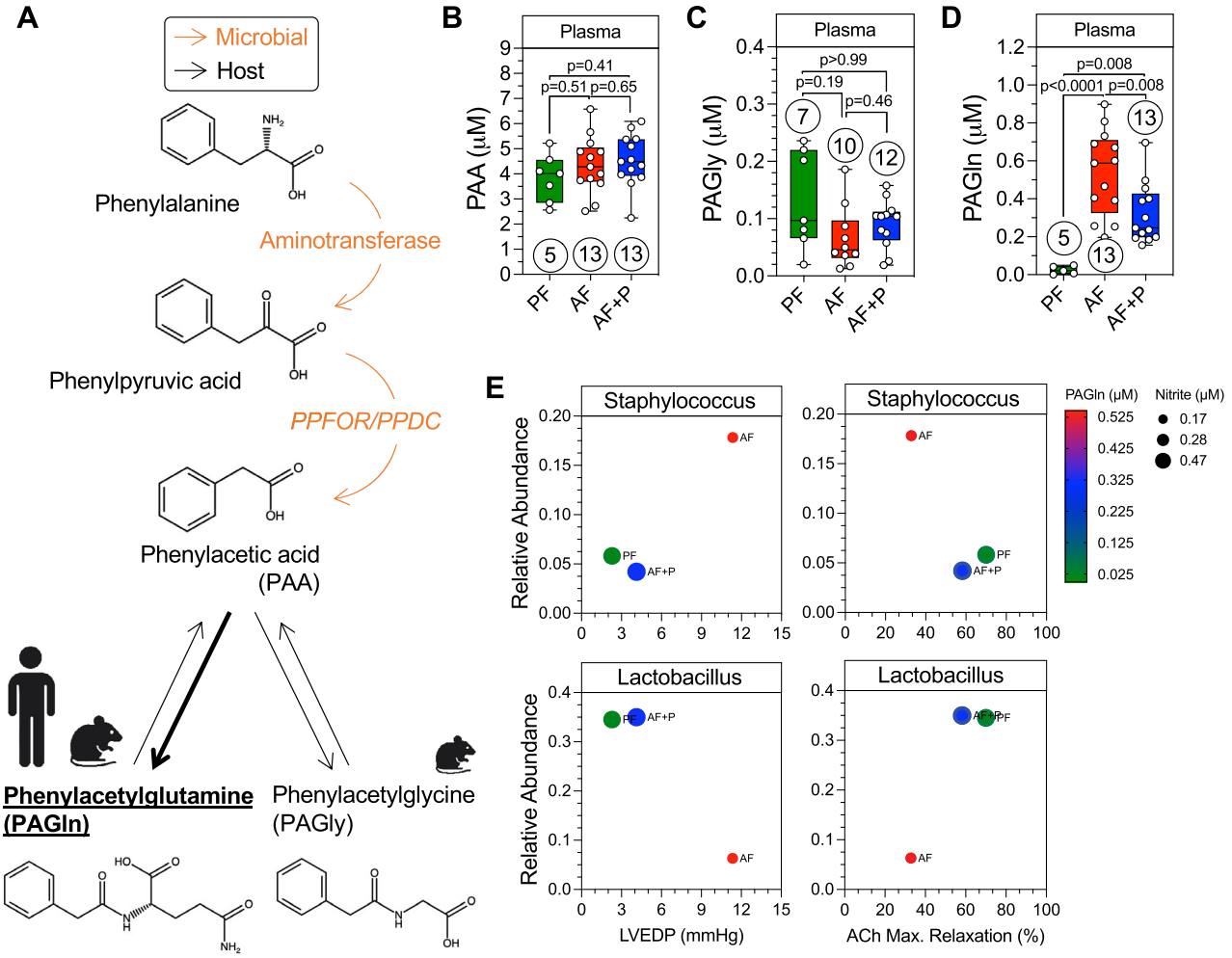

Fig. 4 | Elevated PAGln is associated with cardiac and vascular pathophysiology. A Representative illustration of phenylalanine metabolism in the gut and host to generate phenylacetylglycine (PAGly) or phenylacetylglutamine (PAGln). Microbiome-mediated metabolism (orange) and host-mediated metabolism (black). Created in part by BioRender. Sharp, T. (2024) https://BioRender.com/i94x574. **B**–**D** Plasma phenylacetic acid (PAA), PAGly, and PAGln levels measured by LC-MS/MS. Pair-fed (PF, green); alcohol-fed (AF, red); alcohol-fed + probiotics L3B2 (AF + P, blue). Number of mice enrolled in each measurement is found in open circle from a single experiment. All data are presented as box and whisker plots (mean, max, and min.) with individual measurement dot plots. Significance ($p < 0.05$) was determined by Kruskal-Wallis Test, Dunn's multiple comparisons test (two-sided) unless stated otherwise. **E** Association of mean relative abundance of *Staphylococcus*, plasma PAGln and nitrite levels, and either LVEDP or ACh. Maximal relaxation. Association of mean relative abundance of *Lactobacillus*, plasma PAGln, and nitrite levels, and either LVEDP or ACh. Maximal relaxation.

of all GMMs measured can be found in Supplementary Table 2 (28 in total) and Supplementary Table 3 (PAGly and PAGln), respectively. The above results would collectively suggest that BoCA, in part, leads to gut microbiome reorganization, which increased gut-host production of PAGln.

To understand the relationship between circulating PAGln levels, physiological indicators of cardiac and vascular function, and microbial species found in the gut microbiome, we plotted four-way associations of the mean circulating PAGln levels (color schematic), plasma nitrite levels (symbol size), relative abundance of *Staphylococcus* or *Lactobacillus* and either LVEDP or ex vivo maximal relaxation (Fig. 4E). In AF mice, there was increased relative abundance of pathogenic *Staphylococcus*[36], increased circulating PAGln levels, reduced nitrite, elevated LVEDP and reduced endothelial-dependent vasorelaxation (Fig. 4E, top two panels). Conversely, when the relative abundance of *Lactobacillus*, an integral member of a stable gut microbiome[37], is higher in the PF and AF + P cohorts, we observed overall lower PAGln and LVEDP, and preserved vasoreactivity (Fig. 4E, bottom two panels). Following this clear dichotomy, we designed studies to provide evidence of the causal relationship between the gut microbiome, PAGln accumulation, and aberrant cardiovascular physiology independent of direct alcohol exposure.

Alcohol-associated PAGln production and cardiovascular dysfunction are transmissible traits

To address the relative contribution of alcohol-induced gut microbial reorganization towards increased PAGln levels and subsequent cardiovascular dysfunction, we performed microbial transplantation of gut commensals from PF and AF mice into naïve mice using a previously reported protocol with modifications as described (Fig. 5A)[38]. With AF fecal microbiota transplantation (FMT), we observed an increased trend ($p = 0.076$) mortality as compared to PF controls (Supplementary Fig. 3a). Similar to BoCA findings, there was no significant difference in cardiac structure and function via echocardiography (Fig. 5B–D, Supplementary Table 3). Systemic blood pressure was unchanged in FMT mice, independent of donor (Fig. 5E); however, the mean LVEDP was significantly elevated (Fig. 5F, Supplementary Table 4) in AF-FMT group, confirming the intriguing hemodynamic

https://doi.org/10.1038/s41467-024-55084-2

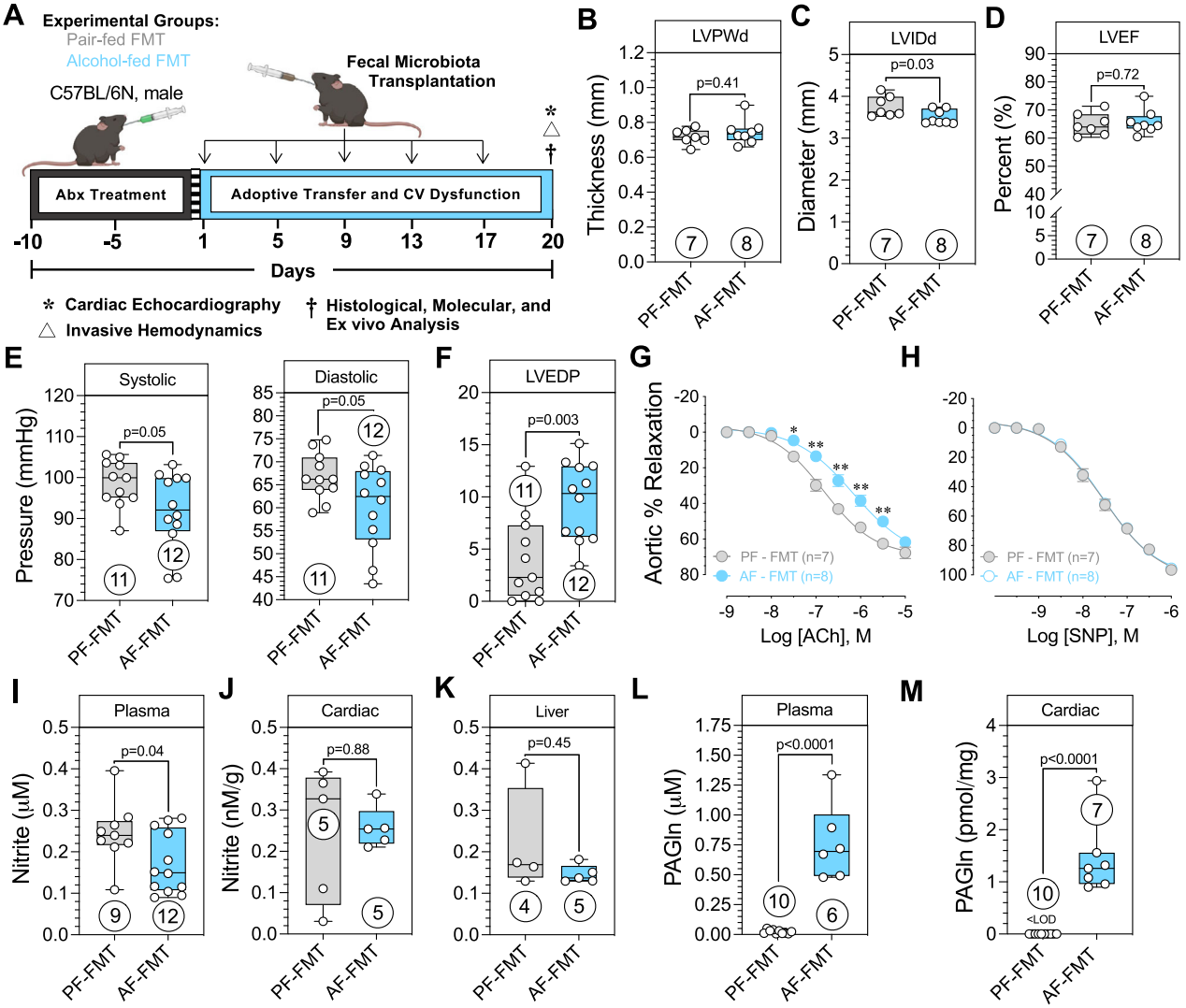

Fig. 5 | Alcohol-associated PAGln production and cardiovascular dysfunction are transmissible traits. A Experimental protocol of fecal microbiota transplantation (FMT) model. Two treatment cohorts were enrolled; pair-fed (PF-FMT, gray); and alcohol-fed (AF-FMT, blue). Created in BioRender. Sharp, T. (2024) https://BioRender.com/x77k051. **B**–**D** Echocardiographic measurements of structure and function. LVPWd left ventricular posterior wall-diastole. LVIDd left ventricular internal diameter-diastole. LVEF, left ventricular ejection fraction. **E** Systemic invasive hemodynamics, systolic and diastolic blood pressure. **F** Left ventricular end-diastolic pressure. **G**, **H** Aortic vasorelaxation to acetylcholine (ACh) and sodium nitroprusside (SNP). Statistical significance ($p < 0.05$) analysis was determined by repeated measures two-way ANOVA with a Bonferroni's multiple comparisons test (two-sided). (*) p-value < 0.05; (**) p-value < 0.01, PF-FMT vs. AF-FMT [blue line], respectively. Non-linear fit lines for each treatment were plotted using log(agonist) vs. response four-parameter variable slope. **I**–**K** Plasma, cardiac, and liver nitrite levels. **I** Plasma PAGln levels measured via LC-MS/MS. **M** Cardiac LC-MS/MS PAGln levels. All data (**B**–**F**, **I**–**M**) are presented as box and whisker plots (mean, max, and min.) with individual measurement dot plots unless otherwise stated from a single experiment. Number of mice enrolled in each measurement is found in open circle. Significance ($p < 0.05$) was determined by nonparametric Mann-Whitney Test compare ranks (two-sided) unless stated otherwise.

findings of the BoCA study. Despite elevated filling pressures, the LV systolic pressure and relaxation time constant Tau were unchanged (Supplementary Fig. 3b, c). Endothelial-dependent vasorelaxation was significantly blunted in groups that received AF- versus PF-FMT groups (Fig. 5G), despite maximal relaxation remaining unchanged (Supplementary Fig. 3d). The rightward shift in the relaxation curve of AF-FMT vessels is indicative of a disruption in the endothelial mediated signaling necessary for vasorelaxation[39]. There was no significant difference in endothelial-independent vasorelaxation to increasing doses of sodium nitroprusside, or in the maximal relaxation between vessels from PF- or AF-FMT cohorts (Fig. 5H and Supplementary Fig. 3e). The antioxidant capacity of those in the AF-FMT cohort was significantly compromised through measurement of 8-isoprostane levels (Supplementary Fig. 3f). Given the ex vivo endothelial-dependent dysfunction, we measured nitrite levels in plasma, cardiac, and liver specimens from each group. Plasma nitrite was significantly lower in those colonized with AF commensals over the 20-day protocol (Fig. 5I). When investigating tissue levels, the hearts and livers of AF-FMT mice had no change in nitrite (Fig. 5J, K). While organ-specific nitrite was not affected, the global circulating reduction in nitrite indicates endothelial dysfunction as described previously[22].

Given the gut microbiota-dependent production of PAGln, we next performed targeted metabolite profiling on plasma and other cardiovascular-related organs. PAGln levels were negligible in all tissues and plasma recovered from recipients of PF-FMT. In contrast we observed markedly increased PAGln levels in those colonized with donor commensals from AF mice (Fig. 5L). Cardiac, liver, and kidney PAGln levels were also significantly increased in AF-FMT compared to PF-FMT counterparts (Fig. 5M, S3G and Supplementary Fig. 3h). Notably, there was no change in plasma of the precursor PAA (Supplementary Fig. 3i) or plasma and tissue PAGly levels (Supplementary Fig. 3j–m), indicating distinct fecal microbial transplanted

https://doi.org/10.1038/s41467-024-55084-2

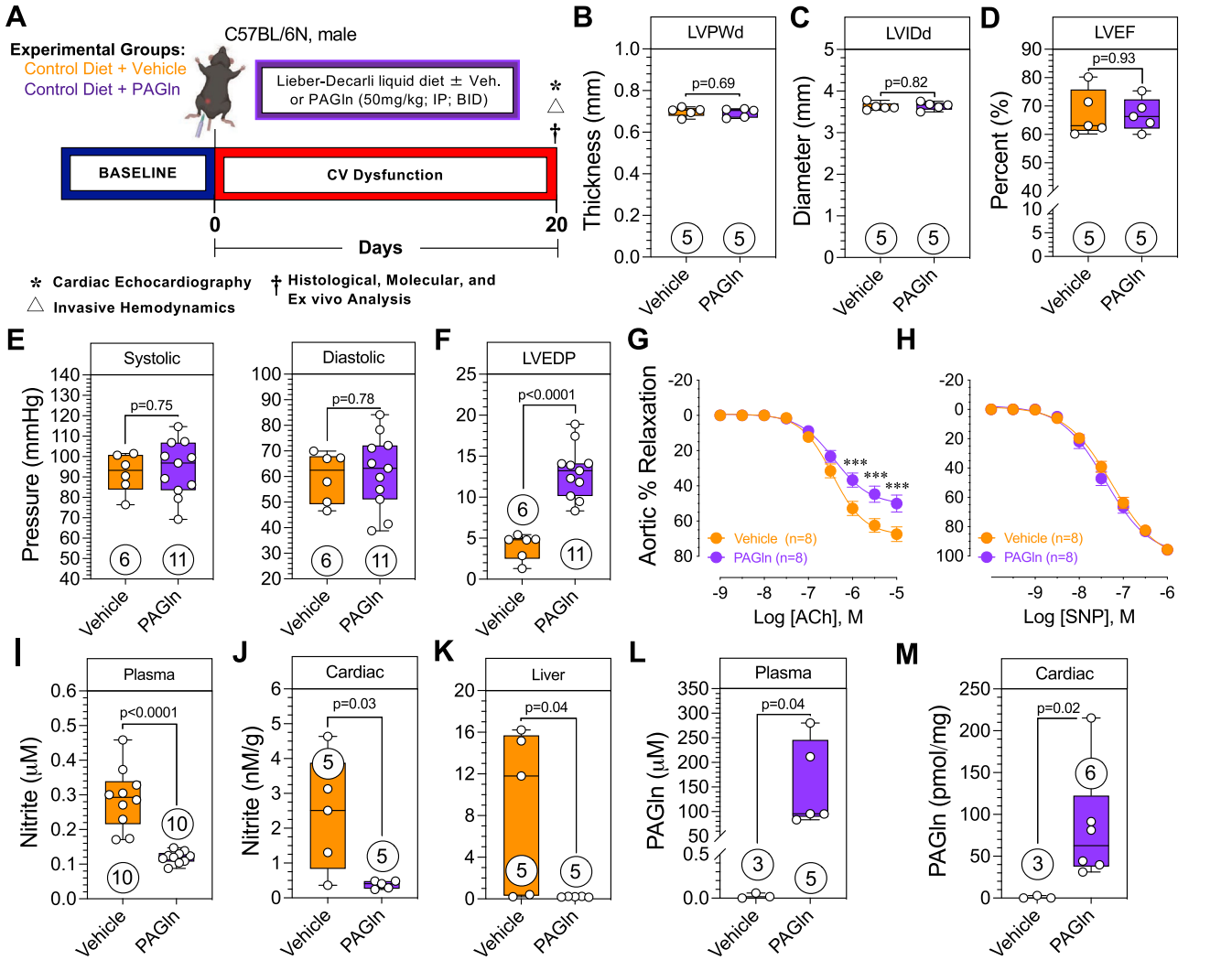

Fig. 6 | PAGln is sufficient to cause cardiovascular dysfunction. A Experimental protocol of pharmacological increases in PAGln. Two treatment cohorts were enrolled: vehicle, orange; and PAGln (50 mg/kg; twice daily, I.P., purple). Created in BioRender. Sharp, T. (2024) https://BioRender.com/x77k051. **B**–**F** Echocardiographic measurements of structure and function. LVPWd left ventricular posterior wall-diastole. LVIDd left ventricular internal diameter-diastole. LVEF left ventricular ejection fraction. **E** Systemic invasive hemodynamics, systolic and diastolic blood pressure. **F** Left ventricular end-diastolic pressure. **G**, **H** Aortic vasorelaxation to acetylcholine (ACh) and sodium nitroprusside (SNP). Statistical significance ($p < 0.05$) analysis was determined by repeated measures two-way ANOVA with a Bonferroni's multiple comparisons test (two-sided). (***) p-value < 0.001 Vehicle [orange line] vs. PAGln [purple line]. Non-linear fit lines for each treatment were plotted using log(agonist) vs. response four-parameter variable slope. **I**–**K** Plasma, cardiac, and liver nitrite levels. **L**, **M** Plasma and Cardiac PAGln levels measured via LC-MS/MS. All data (**B**–**F**, **I**–**M**) are presented as box and whisker plots (mean, max, and min.) with individual measurement dot plots unless otherwise stated from a single experiment. Number of mice enrolled in each measurement is found in open circle. Significance ($p < 0.05$) was determined by nonparametric Mann-Whitney Test compare ranks (two-sided) unless stated otherwise.

communities were differentially impacting host hepatic conjugation enzyme activity, substantially altering the distribution of PAA conjugated metabolites (PAGln vs PAGly) produced. Collectively, the FMT study provides evidence that the alcohol-induced gut microbial reorganization is sufficient to cause the cardiac and vascular dysfunction associated with BoCA consumption. Moreover, the GMM PAGln continues to be implicated in affecting host physiology.

PAGln is sufficient to drive cardiovascular dysfunction

Following the FMT studies demonstrating that alcohol-induced gut microbial reorganization was sufficient to cause CV dysfunction, we pursued studies to investigate the effects of PAGln on cardiac and vascular physiology. In these studies, we performed direct PAGln (50 mg/kg) or vehicle (sterile saline) intraperitoneal injections twice daily for 20 days (Fig. 6A). There was no significant change in mortality (Supplementary Fig. 4a). A subset of animals underwent echocardiographic structure and functional assessment. There were no changes in those treated with PAGln (Fig. 6B–D, Supplementary Table 5). This is unsurprising given the short study timeline and the time needed for cardiac remodeling to occur. The systemic hemodynamic profile and left ventricular filling pressures were similar to those observed in BoCA and FMT studies with no significant changes in the systolic or diastolic blood pressure (Fig. 6E), yet we observed significantly elevated LVEDP in the PAGln treated cohort (Fig. 6F, Supplementary Table 5). Vascular relaxation in an endothelial-dependent manner was dysfunctional, including the maximal relaxation despite no change in smooth muscle-dependent vasorelaxation (Fig. 6G, H, Supplementary Fig. 4d, e). Strikingly, global and tissue (cardiac and liver) nitrite was abolished in the presence of PAGln (Fig. 6I–K). Given the rapid removal of PAGln from the circulation[11] through renal excretion we measured levels acutely post-injection which were markedly elevated in the plasma (Fig. 6L) and multiple organs including cardiac, liver, and kidney (Fig. 6M, Supplementary Fig. 4g, h). Plasma and tissue levels of the precursor PAA (Supplementary Fig. 4i) and variant PAGly plasma and tissue levels (Supplementary Fig. 4j–m) were also elevated

under these conditions. Intestinal fatty acid binding protein levels, as a marker of gut leak, were unchanged in PAGln-treated animals in comparison to the vehicle cohort (Supplementary Fig. 4n).

This set of experiments not only confirms previous association between PAGln and CVD but also provides in vivo evidence of the direct deleterious effects of PAGln on cardiac and vascular function. Independent of dietary phenylalanine levels or alcohol consumption, the known obligatory gut microbiota-dependent metabolite, PAGln, leads to substantial alterations in central cardiac hemodynamics and vascular dysfunction. These studies indicate a direct causal relationship between PAGln and cardiovascular disease in vivo.

PAGln induces hypercontractility and altered Ca^{2+} handling in cardiomyocytes

The above physiological responses suggest that despite the lack of cardiac dysfunction as measured by echocardiography, there is a central effect of PAGln on the ability of the myocardium to contract and relax properly, manifesting as an elevation in LVEDP despite no change in afterload. In preliminary studies, we examined isolated primary murine cardiomyocytes exposed to varying concentrations of PAGln (Supplementary Fig. 5). At multiple concentrations there was hypercontractility as measured by cardiomyocyte sarcomere fractional shortening and its derivatives in response to repetitive field stimulation (Supplementary Fig. 5a–h). Representative transient calcium tracings and quantification show altered peak calcium transients (Supplementary Fig. 5i–p). Given the augmentation of sarcomere shortening and calcium transients, we measured the phosphorylation of phospholamban at residue serine 16 (Ser^{16}), a sarco(endo)plasmic reticulum Ca^{2+}-ATPase (SERCA2a) regulatory protein responsible for the disinhibition through PKA-mediated adrenergic signaling[40]. We observed an absence of $pSer^{16}$ at varying concentrations of PAGln (Supplementary Figs. 5q, r and 6a). We confirmed activation of this conical adrenergic-driven pathway with 10 nM isoproterenol stimulation and were able to inhibit isoproterenol-induced $pSer^{16}$ with carvedilol (β1, β2, and α1 adrenergic receptor inhibitor)[41] preincubation.

PAGln's inability to elicit $pSer^{16}$ of phospholamban was intriguing given the seminal work showing PAGln-mediated effects on platelets act through adrenergic receptor signaling[11]. In a subsequent set of studies, we subjected isolated cardiomyocytes to either isoproterenol or PAGln (2 μM) ± carvedilol (1 μM) and measured cardiomyocyte contraction, calcium transients, and $pSer^{16}$ phospholamban (Fig. 7). PAGln administration confirmed preliminary observations of hypercontractility (Fig. 7B–E) and altered calcium transients (Fig. 7F). Although not significant, PAGln was associated with increased basal calcium (Fig. 7G) suggesting potential diastolic Ca^{2+} regulatory abnormalities. However, peak calcium transients were elevated by PAGln (Fig. 7H). Isoproterenol produced a similar contractile response with no change in basal calcium. In the presence of carvedilol, PAGln-mediated hypercontractility was not inhibited (Fig. 7B–E). Notably, the alterations in PAGln-mediated calcium transients were attenuated in the presence of carvedilol (Fig. 7F–H). Conversely, isoproterenol hypercontractility and calcium transient effects were inhibited with carvedilol pretreatment. This is exemplified by the measure of Tau, the transient decay rate (mediated through PKA phosphorylation of S^{16} phospholamban) (Fig. 7I). Significantly reduced Tau and increased phosphorylation at pS^{16} with isoproterenol administration confirms classical adrenergic-PKA mediated disinhibition of phospholamban, which was inhibited in the presence of carvedilol (Figs. 7J, K, S6B). PAGln did not lead to a reduction in Tau or an upregulation of pS^{16} (Fig. 7J, K) despite increased fractional shortening and peak calcium transients (Fig. 7C, H). These observations suggest an alternative mechanism(s) by which PAGln affects cardiomyocyte contractility and Ca^{2+} handling. Overall, PAGln altered isolated cardiomyocyte contractile and calcium dynamics despite adrenergic blockade, demonstrating the direct effects of PAGln on cardiomyocytes. These data provide the initial evidence supporting the increased left ventricular filling pressures observed in the presence of elevated PAGln in vivo. Moreover, this is the key observation of a potential alternative signaling cascade to the one previously published[11]. Next, we further explored the effects of PAGln on vascular endothelial cells to provide mechanistic insight into ex vivo vascular dysfunction and altered nitric oxide bioavailability.

PAGln induces endothelial cell activation through increased reactive oxygen species leading to endothelial dysfunction

To elucidate vascular endothelial dysfunction, we cultured HCAECs and exposed them to varying concentrations and durations of PAGln (Fig. 8). We assessed endothelial cell activation (type II) through measurement of proinflammatory markers, cell adhesion markers and antioxidants at the transcription and protein levels (Fig. 8A–G). A single exposure under serum-free conditions to either 20 μM or 100 μM PAGln increased cellular expression of *Tie2* tyrosine kinase and *Il-6* (Fig. 8A). Cellular adhesion molecules including *ICAM-1*, *VCAM-1*, and *ELAM-1* were increased in expression at 20 μM and 100 μM PAGln (Fig. 8B). Cytokine *Cxcl-16* expression was elevated with PAGln (Fig. 8C). *Cxcl-16* signaling has been implicated in various CVDs[42] and related comorbidities, such as renal fibrosis[43] and liver disease[44]. Nuclear factor erythroid 2-related factor 2 (*Nrf-2*) expression was downregulated at 4 h in the presence of PAGln, indicating reduced antioxidant capacity (Fig. 8D). Most notably, *Nos-3* expression was increased in a dose-dependent manner (Fig. 8E), indicating a potential compensatory response to reduced nitric oxide bioavailability observed through nitrite measures in previous studies herein (Figs. 2, 5 and 6).

To better understand PAGln's effects on nitric oxide regulation, we probed for total eNOS and phosphorylation regulatory sites T^{495} and S^{1177} in hepatic tissue homogenates from mice administered PAGln or vehicle (Supplementary Fig. 8). Hepatic specimens were utilized given this being the site of major PAGln formation[35]. Total eNOS was unchanged between cohorts (Supplementary Fig. 8c). Phosphorylation of T^{495} residue on eNOS, which has traditionally been shown as a regulatory site inhibiting eNOS-derived nitric oxide production while promoting eNOS uncoupling and superoxide formation, was increased in animals who received PAGln (Supplementary Fig. 8c)[45]. Conversely, S^{1177} was also significantly elevated in the PAGln cohort liver samples (Supplementary Fig. 8c). S^{1177} is known as a classical activation site and is phosphorylated by a myriad of secondary messengers including CAM kinase II and AKT1-mediated activation independent of intracellular calcium[46]. The increased phosphorylation at T^{495} of eNOS suggests an inhibition of nitric oxide production and reduced bioavailability, while potentially increasing the production of superoxide free radicals and peroxynitrite formation. Furthermore, reduced levels of nitrite in multiple organs, and abnormal vasorelaxation were observed in the BoCA (Fig. 2), FMT (Fig. 5), and PAGln studies (Fig. 6). These findings of increased transcription of cellular adhesion molecules and inhibition of eNOS production of nitric oxide are hallmarks of vascular endothelial dysfunction[47], providing potential mechanistic insight on the connection between gut microbial reorganization, subsequent PAGln production, and their role in the manifestation of vascular dysfunction.

Given the transcriptional expression of classical endothelial cell activation markers, we assessed live cell reactive oxygen species (ROS) in HCAECs over 12-h using a fluorogenic sensor in the presence or absence of PAGln (Fig. 8F) as a driver of the mRNA profile. Over the course of the experiment, we observed an increase in the percentage of GFP^+ area in the PAGln-treated group in comparison to control when normalized to baseline. These data demonstrate increased intracellular ROS in the presence of PAGln, providing insight into a potential

https://doi.org/10.1038/s41467-024-55084-2

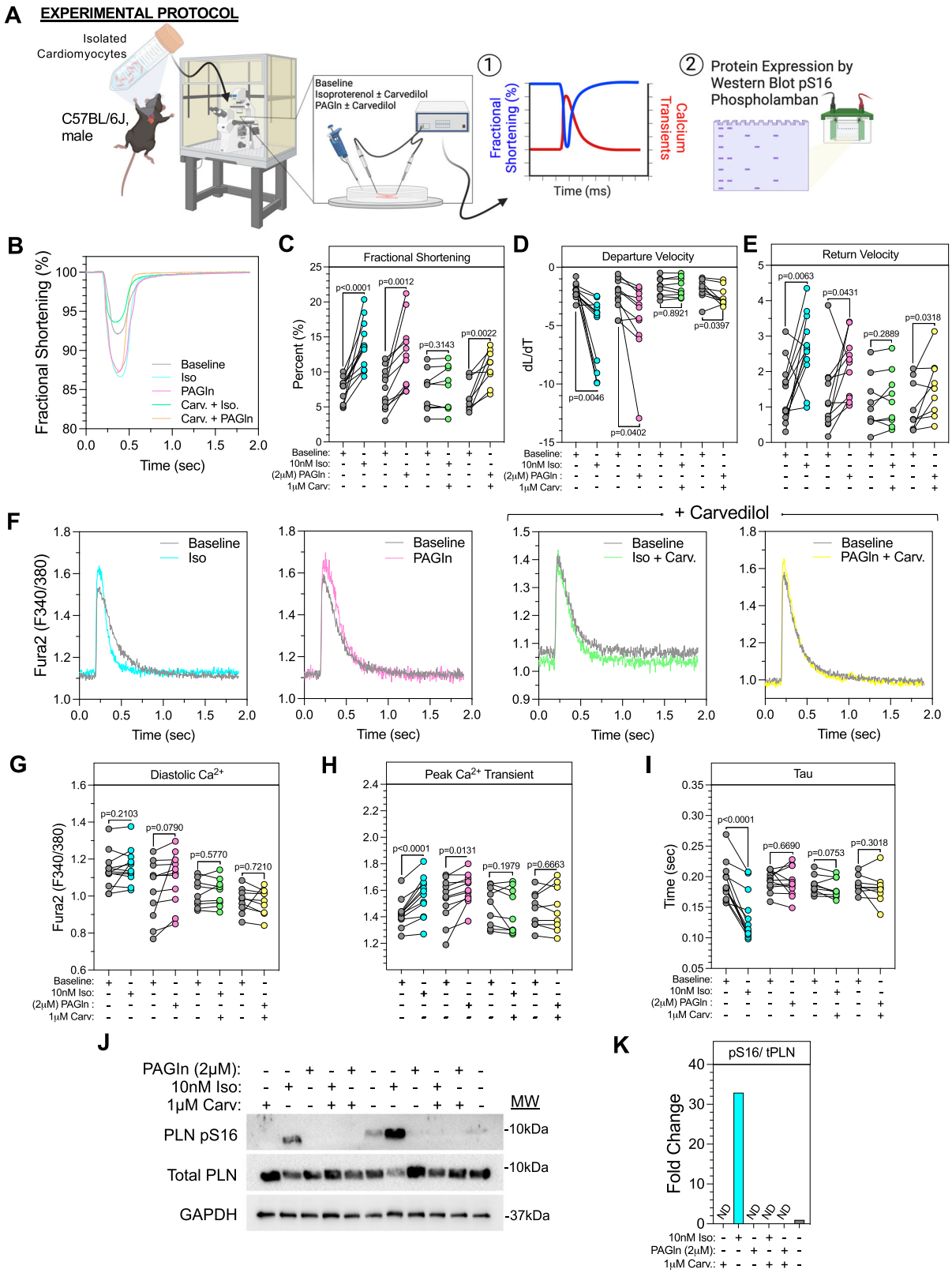

mechanism by which expression of proinflammatory and cell adhesion molecules is increased with PAGln exposure.

In addition to transcriptional markers of endothelial cell activation and increased ROS, we performed protein level analysis of proinflammatory cytokines as well as antioxidants to further elucidate the cellular response to PAGln in a time-dependent manner (Fig. 8G, H) (Supplementary Fig. 7). Proinflammatory cytokines interleukin-1beta (IL-1β) and interleukin-18 (IL-18) were increased in HCAECs exposed to PAGln conditioned media. While IL-1β was only trending, IL-18 was significantly elevated in comparison to vehicle-treated cells (Fig. 8G, H). Classical enzymatic antioxidants (i.e., catalase-1, superoxide dismutase-1 [SOD-1]) and heme oxygenase-1 (HO-1) were assessed for protein expression levels. While catalase-1 was elevated throughout, variation in the vehicle-treated group limited statistical significance. SOD-1 has a modest response across time and compared to vehicle. HO-1 incrementally elevated over 48-h, with a significant

Fig. 7 | PAGln induces hypercontractility and altered Ca^{2+} handling in cardiomyocytes. A Illustration of experimental protocol for isolation and measurement of cardiomyocyte sarcomere length and calcium transients under varying conditions (i.e., baseline [gray]), isoproterenol (iso, 10 nM [light blue]) ± carvedilol (carv., 1 μM [green]), or PAGln (2 μM [pink]) ± carv. (yellow). Created in BioRender. Sharp, T. (2024) https://BioRender.com/v51f310. **B** Representative field stimulation tracings of baseline and exposure to iso. or PAGln ± carv. **C** Sarcomere fractional shortening as a percentage change of baseline. **D**, **E** Departure and return velocities, change in length over change in time. **F** Representative calcium transients during field stimulation at baseline and following exposure to iso. ± carv. or PAGln ± carv. **G** Baseline intracellular diastolic calcium in each condition. **H** Peak intracellular calcium transients in each condition. **I** Tau, transient decay rate, at baseline and after exposure to PAGln. **J**, **K** Phospholamban (PLN) total abundance and phosphorylation (*p*) at serine 16 (S^{16}) normalized to total PLN protein in isolated cardiomyocyte lysate post incubation with PAGln, isoproterenol (10 nM), carvedilol (1 μM), or combination in a single experiment with (2) replicates. Quantification of total PLN and pS^{16} PLN. PAGln phenylacetylglutamine. All data (**C**–**E**, **G**–**I**) are presented as individual independent biological replicate dot plots. Normality was assessed using the Shapiro-Wilk test. Statistical significance ($p < 0.05$) was determined by (two-tailed) unpaired t-Test performed on parametric data sets while Mann-Whitney test was used to compare ranks on nonparametric data unless otherwise stated.

elevation in PAGln conditioned media at 24-h (Fig. 8G, H). The differential response in antioxidant protein levels provides preliminary insight into the type of oxidative stresses that may be produced due to PAGln exposure.

Vascular endothelial cell function is a regulator of homeostatic processes which play roles in angiogenesis, anticoagulation, and overall vessel function[48–51]. Finally, we performed wound healing scratch assays to understand what effect PAGln exposure would have on the complex responses necessary for wound healing. We grew HCAECs to roughly 80–90% confluency and performed scratch assay ± PAGln (100 μM) (Fig. 8I, K). Serial images were collected over the course of 24 h. Representative images a time 0, 12 h post, and 24 h post scratch demonstrate a clear difference in the ability of the cells to migrate and heal the wound in the presence of PAGln (Fig. 8I and Supplementary Fig. 8D). In the vehicle-treated arm, there was an 85% healing of the affected area. In the PAGln treated wells, 73% and 25% healing occurred (24 h or 48 h pre-incubation [inc.], respectively). Linear regression analysis of the three groups demonstrated a significant ($p < 0.0001$) difference among the slopes of each group across 24 h (Fig. 8K).

Collectively, these data provide the earliest evidence, to our knowledge, of direct vascular endothelial effects of PAGln on ROS dynamics, activation of endothelial cells, and alterations to wound healing characteristics. Observations, in vitro, support the consistent in vivo data demonstrating abnormal vascular relaxation and reduced circulating nitrite in the BOCA, FMT, and PAGln studies.

Discussion

Given evidence supporting alcohol production and consumption as early as 7000 B.C., it is critical to understand its ubiquitous role in human society including disease pathology[52]. Moreover, we now understand that CVDs, previously believed to be modern pathologies (i.e., coronary artery), also plaque premodern humans at least 4000 years ago[53]. While our modern association of alcohol with all-cause mortality remains consistent, understanding alcohol's association with CVD has been controversial[54]. Despite previous long-standing notions that mild/moderate consumption of alcohol may offer some health benefits[55] a paradigm shift in our understanding of the relationship between alcohol consumption and CVD has occurred given more recent data that accounts for lifestyle factor[2]. Notably, our findings further support several recent clinical and basic research studies that have reported an association between alcohol and gut dysbiosis[56], alcohol and CVD[57], and elevated PAGln and CV-related diseases[58]. Moreover, we provide the initial evidence of elevated PAGln levels in people with alcohol use disorder. Importantly, in blinded preclinical studies, the analysis revealed elevated PAGln levels were associated with similar detrimental effects on cardiac and vascular function in three distinct models (BoCA, FMT, and PAGln–i.p. model). Methodology and parameters evaluated included echocardiography, invasive hemodynamics, ex vivo vascular reactivity, and nitrite levels. Additionally, our studies provide direct evidence of the cellular-specific consequences of PAGln on cardiomyocyte contractility and vascular endothelial cell activation. This demonstrates a direct link to PAGln's cardiovascular pathophysiological effects.

We explored the relationship between alcohol use in humans seeking treatment for alcohol use disorder and their altered circulating metabolome. We identified PAGln as a significantly altered GMM in comparison to healthy counterparts. Several other GMMs have been identified as altered in patients with alcohol use disorders and have effects on host physiology[8,59]. Furthermore, serum PAGln levels were positively associated with self-reported AUDIT-C scores in HDs demonstrating the burden of excessive alcohol use with altered dietary- host metabolites. Within the enrolled subjects, two-thirds were male and stratification by sex demonstrate a significant increase in men. While a similar trend was observed in females, the limited number of enrolled female subjects should be increased in future studies to provide a better understanding of PAGln's association. Given the multifactorial nature of GMM flux, this clinical study did not take into account the dietary components or time to last meal of individuals enrolled, necessitating the need for further studies with more stringent enrollment criteria. It should also be noted that access to this patient population of excessive drinkers is very challenging. In totality, this is the initial observation to our knowledge that phenylalanine GMM PAGln is associated with alcohol use disorder. Given these observations, we explored the biological and microbial consequences of alcohol on the cardiovascular system.

The initial findings of the BoCA study suggest an association of alcohol-induced alterations in gut microbial structure and function and worsening CV functional outcomes. Yet initially, the direct cellular effects of alcohol as the primary driver of CV dysfunction could not be excluded[60]. The alcohol-induced gut microbial reorganization also provides evidence supporting a growing body of work linking alcohol with gut health[24,61] and gut–host interaction in the context of disease susceptibility[62]. The utilization of L3B2 to induce compositional changes in the microbial community structure suggests alcohol's ability to induce selective pressures that modulate the microbial community[63]. Further evidenced by the changes in microbe damage and death measured in cecal samples. Importantly, the FMT studies we performed verify the fundamental role of the gut microbiome on host physiology, specifically the gut-dependent production of PAGln on host predisposition to CVD. Moreover, these studies reveal that the microbial dysfunction induced by alcohol alone is sufficient to induce increased PAGln production independent of other factors (i.e., dietary enrichment of phenylalanine) that have been utilized in many other studies[64]. Similar findings have been observed with other GMMs such as TMAO, which increases the severity of stroke and functional deficits[65]. As with TMAO[66], it is of interest to initiate studies that target the gut microbiome[67], specifically phenylalanine metabolism and/or PAGln/PAGly production[68], not only in the context of CVD but also for hazardous alcohol use disorders given the present data. In demonstrating that alcohol dysbiosis was sufficient to drive CV pathogenesis, we wanted to explore the direct relationship of PAGln as a primary driver of causality rather than a consequential secondary observation.

Elevated circulating and urinary PAGln levels have been associated with CV-related comorbidities including renal disease[10] and

https://doi.org/10.1038/s41467-024-55084-2

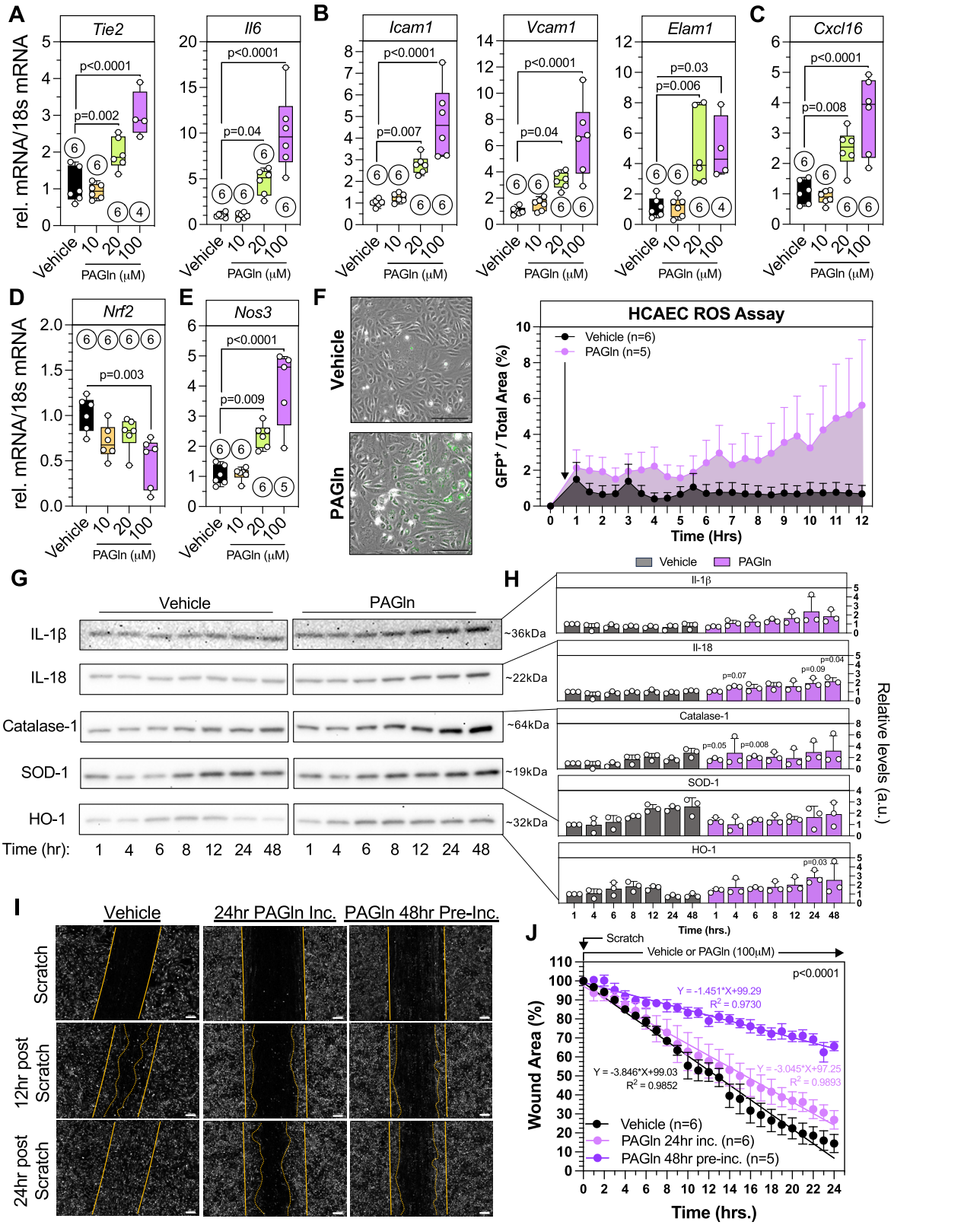

diabetes[11]. Most recently, PAGln has been clinically linked to heart failure[68] and major adverse cardiovascular events[11]. Our data indicate a preferential production of the glutamine-conjugated phenylacetyl-metabolite, providing the initial evidence of a humanized mouse model of gut-derived phenylalanine metabolism. Several factors should be taken into consideration regarding this observation, including differences in experimental protocols, mouse strain, and the microbial diversity of mice enrolled in these studies[69]. Despite the data herein and previous studies linking PAGln to cardiometabolic phenotypes[11], there are limited results providing direct evidence of PAGln's ability to cause cardiac or vascular dysfunction[68]. Independent of both alcohol and gut microbial reorganization, we observed similar cardiac and vascular dysfunction in pharmacological-mediated increases in PAGln-exposed mice compared to those observed in the BoCA and FMT studies. Further, a single previous report provides data that PAGln affected cellular processes through adrenergic receptor

Fig. 8 | PAGln induces endothelial cell activation through increased reactive oxygen species leading to endothelial dysfunction. A–E Messenger RNA expression levels of markers of endothelial cell activation in vehicle (black/gray) or PAGln-treated (10, orange; 20, green; 100, purple). TEK tyrosine kinase (*Tie2*); interleukin 6 (*Il6*); Intercellular adhesion molecule, vascular cell adhesion molecule, and endothelial-leukocyte adhesion molecule (*Icam1*, *Vcam1*, *Elam1*, respectively); – chemokine ligand 16 (*Cxcl16*); nuclear factor erythroid 2-related factor 2 (*Nrf2*); nitric oxide synthase 3 (*Nos3*). Number of independent biological replicates enrolled in each measurement is found in open circle. All data are presented as box and whisker plots (mean, max, and min.) with individual measurement dot plots. Significance ($p < 0.05$) was determined by Kruskal-Wallis Test, Dunn's multiple comparisons test (two-sided) unless stated otherwise. **F** Representative 20× magnified phase-contrast photomicrographs with fluorescent overlay of ROS sensor in HCAECs under three conditions: (1) control or (2) PAGln (100 µM, purple) incubation. Quantification of GFP^+ as a percentage of total image normalized to baseline (time 0). $N = 5–6$ independent biological replicates were performed per treatment. Plotted the mean + SEM with group across time. Shaded area represents the total area under the curve per treatment group. Scale bar = 200 µm. **G**, **H** Representative western blot images of interleukin-1B, interleukin-18, catalase-1, superoxide dismutase-1 (SOD-1) and heme oxygenase-1 (HO-1) across time in vechile-treated or PAGln-treated HCAECs ($n = 3$ independent biological replicates [i.e., wells], each per timepoint per condition). Relative abundance of the vehicle, normalized to vehicle 1-h and PAGln-treated HCAECs normalized to the respective vehicle timepoint. Data are presented as the mean ± SEM. Dot plots show independent biological replicates. Multiple student *t*-test (two-tailed) were performed for statistical significance ($p < 0.05$) analysis. **I**, **J** Representative 4× magnified photomicrographs of scratch assay wells from vehicle (black), 24 h PAGln incubation (light purple), and PAGln 48 h pre-incubation (inc.)(dark purple) at baseline, 12-h post, and 24-h post injury. $N = 5–6$ independent biological replicates were performed per treatment. Quantification of wound healing as a percentage of original scratch over 24-h presented as the mean ± SEM. Linear regression analysis was performed for each condition to provide the slope and y-intercept for each condition. Significance ($p < 0.05$) was determined for the slope between groups. Scale bar = 200 µm.

signaling on platelets, leading to increased thrombus formation and the potential for worsening CV outcomes[11]. Additionally, a report of preliminary experiments in isolated murine cardiomyocytes suggests both PAGln and PAGly can promote inhibitory effects on ex vivo cardiomyocyte sarcomere shortening in the presence of catecholamines and induce BNP (*Nppb*) gene expression in vitro and in vivo[68]. Beyond these observations, there is a paucity of mechanistic insights linking PAGln to cardiac and vascular pathology, specifically cardiomyocytes and endothelial cellular physiological responses.

Previously reported findings of PAGln showed no effect on cardiomyocytes in isolation, but demonstrated negative allosteric behavior with reduced catecholamine-stimulated responses[68]. However, we observed hypercontractility when we exposed isolated cardiomyocytes to varying concentrations of PAGln (0.5–200 µM) during continuous field stimulation. Hypercontractility in cardiomyocytes would traditionally indicate signaling through a classical adrenergic receptor PKA-mediated cascade, wherein pS^{16} phospholamban increases, leading to disinhibition of SERCA2a, increased sarcoplasmic reticulum Ca^{2+} store, and subsequent increased fractional shortening. In our studies, concentration-dependent exposure to PAGln led to altered diastolic calcium and/or increased calcium transients, but no upregulation in the phosphorylation of SERCA2a regulatory protein phospholamban. With no effect of carvedilol on PAGln-induced hypercontractility, there is an opportunity to investigate novel alternative signaling mechanism(s) which could be mediating PAGln's cardiomyocyte effects. Although not explored in the present studies, several alternative mechanisms such as fundamental changes in sarcomere myofilament dynamics[70], or modification to other calcium regulatory sites (ryanodine receptor, L-type calcium channel, Na^+/Ca^{2+} exchanger, or Na^+/K^+ ATPase)[71] could underlie the observed PAGln-mediated increases in myocyte contractility and altered calcium homeostasis. To our knowledge, this is the initial report demonstrating PAGln's ability to alter cellular physiological response independent of previously reported adrenergic-dependent signaling. The hypercontractile nature and altered calcium regulation observed ex vivo provide insight into the inability of the myocardium to relax properly, thereby potentially leading to elevations in LV filling pressures in vivo. This type of cardiac dysfunction is reminiscent of hypertrophic cardiomyopathy[72], despite not observing this phenotype in our models due to the limited exposure of 20 days. Chronic studies would be necessary to determine whether PAGln-dependent cardiac remodeling would occur.

The cardiovascular system is highly regulated by vascular function, both at the level of the myocardium[73] and systemically[74]. Endothelial cell activation is an early and critical sign in the pathogenesis of numerous CVDs, including vascular disease. Endothelial activation is in part defined by the expression of pro-inflammatory cytokines, cell adhesion molecules (i.e., expression of *Il-6*, *Tie2*, *Cxcl-16*, *Icam-1*, *Vcam-1*, and *Elam-1*)[75], and disruption of canonical nitric oxide signaling[76]. These perturbations can ultimately render the vasculature prone to atherosclerosis and increase thrombus formation, leading to major adverse cardiovascular events. Given that disruption in nitric oxide bioavailability is an early hallmark of endothelial dysfunction and activation[77], the recapitulated observation of altered endothelial-dependent vasorelaxation and global reductions in nitrite in all studies led us to investigate the direct effects of PAGln on HCAECs. Similar to tumor necrosis factor-α and interleukin-1β[78], PAGln initiated the transcriptional activation of numerous adhesion molecules and proinflammatory cytokines while down-regulating an antioxidant defense system evidenced by reduced *Nrf-2* expression. Interestingly, there was an increase in *Nos-3* expression in HCAECs, which could be a result of compensatory mechanisms in response to decreased nitric oxide production and initial endothelial injury due to PAGln exposure. However, under deleterious conditions such as high oxidative stress, some eNOS post-translational modifications promote uncoupling and production of superoxide, potentially further compounding PAGln-induced detrimental impacts[79].

Despite increased *Nos-3* mRNA expression in cells, we sought to further explore eNOS protein regulation at the post-translational modification, tissue homogenates revealed an increase in T^{495} phosphorylation, suggesting classical eNOS inhibition of nitric oxide production. More intriguingly, there was increased S^{1177} in PAGln-exposed mice. The increased phosphorylation at both sites is unpredicted. When examining S^{1177} phosphorylation in a nuanced manner, others have hypothesized that this site does not necessarily lead to activation but increased sensitivity at lower levels of calcium[80]. Furthermore, multispectral imaging and chemogenetic methods have shown discordance between activation of eNOS through S^{1177} phosphorylation and nitric oxide synthesis in vitro[81]. Others have also reported the dephosphorylation of T^{495} precedes the phosphorylation of S^{1177} upon activation of eNOS[45]. It is plausible that in our studies, the persistent phosphorylation of T^{495} induced by PAGln exposure rendered the phosphorylation of S^{1177} ineffective.

With increased transcriptional expression and inconclusive results regarding eNOS regulation, we sought to determine if PAGln induces ROS formation in vitro. We performed live cell microscopy using a fluorometric sensor for ROS in HCAECs over a 12-h exposure to PAGln-conditioned media. PAGln elicited a ROS response providing evidence of a high oxidative stress environment which may, in part, be responsible for transcriptional endothelial cell activation[82]. Furthermore, there was a gradual increase in original IL-1 family members, IL-1β, and IL-18 protein levels in HCAECs exposed to PAGln. These two interleukins are closely related due to the common inflammasome-mediated proteolytic pathway which necessitates the cleavage of a pro-precursor into the active cytokine[83]. Il-1β and IL-18 expression are driven by pathogen- and damage-associated molecular patterns

(PAMPs and DAMPS), as well as other proinflammatory cytokines including interferon-gamma[84,85]. IL-18 has classically been described as an enhancer of the immune response by promoting interferon-gamma expression among other downstream consequences[83]. While originally thought to be macrophage exclusive, recent studies have demonstrate expression of IL-18 in most barrier epithelia and ongoing research seeks to unravel the pleiotropic nature of IL-18 as both an effector and potential a preformed alarmin sequestered in cells to be released rapidly in response to proinflammatory signaling[86]. The significant elevation of IL-18 in HCAECs exposed to PAGln-conditioned media suggests that PAGln may activate similar PAMP/DAMP signaling cascades and drive increased protein expression of this effector or alarmin interleukin.

We also investigated the temporal changes in HCAEC antioxidant levels with exposure to PAGln-conditioned media. We observed an early and sustained increase, although not significant, in catalase-1, a classic enzymatic antioxidant[87]. Additionally, heme oxygenase-1 (HO-1) gradually increased with time, becoming significant at 24-h post exposure. HO-1 is the inducible isoform of heme oxygenase upregulated in most cells in response to increased levels of ROS and is thought to be a counterbalance to the pro-oxidant stimuli[88]. Preclinical and clinical studies have demonstrated the necessity of HO-1 functionality in order to maintain proper ROS balance[89–91]. Moreover, clinical evidence has demonstrated that HO-1 deficiency leads to increased ROS levels resulting specifically in endothelial cell injury in these patients[90]. Herein, HCAECs exposed to PAGln conditioned media induced increased HO-1 expression providing further evidence of the pro-oxidant nature of PAGln. This suggests an attempt by the HCAECs to mount a response to the increased ROS in order to maintain homeostatic ROS balance[92,93].

Longitudinal effects of alcohol on the gut microbiome and its relationship to subsequent CVD have not been investigated in preclinical or clinical studies. Furthermore, a paucity of data exists on temporal exposure to alcohol in the context of a major adverse cardiovascular event such as myocardial infarction (before, during, and after). All preclinical animal models have challenges and limitations in replicating human physiology, therefore translation of alcohol's effects on the gut microbiome and associated PAGln production may be limited. Further clinical studies are necessary to validate and provide more insight into the relationship between alcohol-induced PAGln and CVD. While we have demonstrated the direct physiological effects of PAGln on specific CV cell types, further investigation is needed to fully elucidate signaling cascades which mediate cellular-specific responses. Future studies are required to elucidate endothelial- and cardiomyocyte-specific cell signaling cascades in the presence of PAGln. The observation of aberrant cardiomyocyte contractility and calcium handling, along with endothelial cell activation and inhibition of nitric oxide bioavailability are widely reported as early markers of cardiovascular dysfunction and disease manifestation[94].

Our results show the association of elevated PAGln levels in people living with alcohol use disorders, and that alcohol-dependent dysregulation of gut homeostasis contributes to functional impairment in the cardiovascular system (Fig. 9). Moreover, these disease-associated phenotypes were transmissible with gut microbial transplantation to naïve recipient mice. Upon further examination, the alcohol-induced microbial reorganization was shown to result in excessive generation of pathological gut-derived PAGln in the host, which impacts host cardiac and vascular function (Fig. 9). It is of interest both clinically and for our fundamental understanding of alcohol-related organ damage that targeting of the gut microbiome with probiotic supplementation can augment the deleterious liver and cardiovascular effects of alcohol consumption. The present studies, when taken together with previous work associating PAGln with CVD, suggest that dietary and gut-centric interventions in subjects with a history of alcohol use disorder and/or increased risk of CVD warrant further exploration, despite potential theoretical difficulties due to PAGln production pathway redundancy[35]. The combined findings from these studies highlight the profound relationship between the largest modifiable risk factor-our dietary intake-and its impact on host pathophysiology, partly mediated through gut-centric metabolic pathways and GMMs.

Methods

Experimental models and details

Human serum samples. A total of 126 heavy drinkers with an Alcohol Use Disorders Identification Test (AUDIT) score greater than eight were enrolled at the Fairbanks Drug and Alcohol Treatment Center (Indianapolis, IN), as previously described, written informed consent was obtained from subject involved in the study[13]. Additionally, 22 healthy controls with no known history of excessive drinking were recruited[13]. At enrollment, demographic information, clinical characteristics, and laboratory tests were collected[13]. Blood samples were collected, and centrifuged at 1500 *g* for 10 min at 4 °C, and the serum was stored at −80 °C until analysis. The study design was approved by the institutional review boards at Indiana University-Purdue University Indianapolis, Fairbanks Alcohol Rehabilitation Center, and Roudebush Veterans Administration Medical Center. Serum preparation and analysis were conducted at Metabolon (Durham, NC), as previously detailed[13,95,96]. Metabolites were identified by comparing ion features in the experimental samples to a reference library of chemical standards, which included retention time, molecular weight (*m/z*), preferred adducts, in-source fragments, and associated MS spectra[13].

Mice and experimental protocols. Ten-week-old C57BL6/N male mice, with initial body weights of ~25 g (Charles River, MA, USA) were maintained in specific pathogen-free facilities at Louisiana State University Health Science Center−New Orleans, Department of Animal Care. Mice were housed in filtered top cages, fed sterile food and water until enrolled in specific studies and kept under standard environmental conditions (25 °C, 56% humidity, 12-h light cycle) throughout the duration at LSUHSC-NO. Animals were enrolled in one of three studies: (1) binge-on-chronic alcohol ± probiotics L3B2, (2) fecal microbiota transplantation study, or (3) pharmacological-mediated increase in host phenylacetylglutamine studies. All experiments were reviewed and approved by the LSUHSC and USF Institutional Animal Care and Use Committee.

Binge-on-Chronic Alcohol (BoCA). The binge-on-chronic alcohol (BoCA) model was adopted from the NIAAA model[97]. Animals in this model were subjected to chronic alcohol consumption for 20 days, in addition to two binges of alcohol every tenth day. Animals were acclimated to a Lieber-DiCarlo control liquid diet (#F1259; Bio-serv, New Jersey, USA) for 5 days. Animals were then randomized to specific treatment groups. Those in the pair-fed control group ($n = 28$) remained on the Lieber-DiCarli control liquid diet. The amount of control diet given to the pair-fed control animals was adjusted daily to the food intake of animals receiving the alcohol diet. Those animals randomized to any group with ethanol consumption (alcohol control [$n = 47$] or alcohol + probiotics L3B2 [$n = 42$] were placed on a Lieber DiCarli ethanol diet (#F1258, Bio-serv, New Jersey, USA) (5% ethanol, vol/vol) for the remainder of the study. Food was prepared daily and exchanged between 16:00 and 17:00 pm. Two alcohol binges (4 g/kg) were given via gavage in the 20-day study, day 10 and 20, respectively, to all groups. Mice were subjected to terminal procedures and euthanized 9 h after the final binge.

Probiotic administration. In the AF + P group, a combination of probiotic microbes, as previously described[98], consisted of five live species within the *Lactobacillaceae* and *Bifidobacteriaceae* families: *Lactobacillus plantarum*, *Lactobacillus reuteri 1E1*, *Lactobacillus rhamnosus*, *Bifidobacterium bifidum,* and *Bifidobacterium lactis* (L3B2).

https://doi.org/10.1038/s41467-024-55084-2

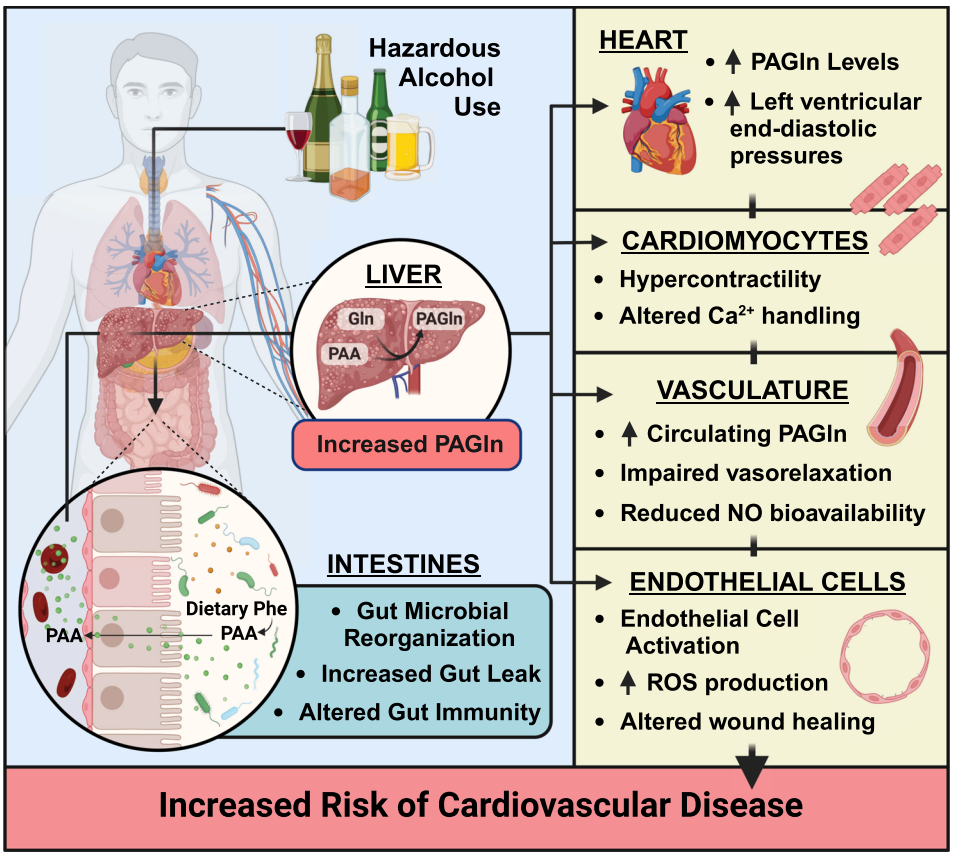

Fig. 9 | Illustration summarizing how alcohol-induced microbial reorganization and associated phenylacetylglutamine production leads to cardiovascular disease. Consumption of alcohol leads to various pathological alterations in the gut including microbial reorganization, loss of gut barrier function, and altered gut immunity. Furthermore, this leads to an increase in host levels of phenylacetylglutamine (PAGln) which through fecal transplant studies and direct injection demonstrates consistent pathophysiological effects similar to that of alcohol on the cardiovascular system—including the heart, cardiomyocytes, vasculature, and endothelial cells. These results provide a gut-centric mechanism by which alcohol consumption leads to increased susceptibility to cardiovascular disease. Created in BioRender. Sharp, T. (2024) https://BioRender.com/q32a230.

These were combined under sterile conditions as lyophilized powder at a known CFU/g concentration (10^8 CFU/ml; 1:1:1:1:1 ratio) (Dupont, Delaware, USA) in sterile water. This was made fresh and added to the Lieber-DiCarli ethanol diet daily for those animals enrolled in the AF + P group.

Fecal microbiota transplantation (FMT). FMT was performed as previously described[99]. Mice were maintained on a Lieber-DiCarli control liquid diet and treated by oral gavage (100 µl/day) for 10 days with an antibiotic cocktail (0.25 mg/mouse/day ampicillin, 0.25 mg/mouse/day gentamicin, 0.25 mg/mouse/day metronidazole, 0.25 mg/mouse/day neomycin and 0.125 mg/mouse/day vancomycin). After antibiotic treatment, mice were randomized to receive pair-fed ($n = 20$) or alcohol-fed ($n = 19$) fecal microbiota. The cecal material from the previously described BoCA study was collected upon euthanasia from the pair-fed and alcohol-fed controls and homogenized (1:5 wt/vol) in sterile 0.5% L-cysteine containing phosphate-buffered saline. The slurry was then separated through centrifugation (80 g, 10 min, 4 °C) to remove large organic contaminants and stored at −80 °C until administered. FMT (200 µl/dose) occurred on days 1, 5, 9, 13, and 17 in a 20-day-long study to mimic the exposure time to alcohol as set forth in the BoCA studies. Three days after the last FMT dose mice underwent terminal procedures and tissue harvesting for molecular and biochemical analysis.

PAGln administration. Mice were acclimated and maintained a Lieber-DiCarli control liquid diet throughout the study. PAGln (50 mg/kg) (Santa Cruz, TX, USA) or sterile water vehicle was administered through intraperitoneal injection twice daily (8:00 h and 16:00 h) for 20 days. On day 20, mice underwent terminal procedures and tissue harvesting for molecular and biochemical analysis.

Primary cardiomyocytes. Left ventricular cardiomyocytes were isolated from adult (8–12-week-old) C57BL/6J mice for cell physiology experiments. Cardiectomy was performed under general anesthesia. Hearts were rapidly excised and mounted to a constant flow Langendorff perfusion apparatus via cannulation of the aorta. Perfusion digestion was performed at 37 °C with Tyrode's solution (10 mM glucose, 5 mM HEPES, 5.4 mM KCl, 1.2 mM $MgCl_2$, 150 mM NaCl, 2 mM sodium pyruvate, pH 7.35) containing 180 U/mL Collagenase Type II (Worthington #LS004177), 10 mM Taurine, and 12 mM 2,3-Butanedione monoxime. Following digestion, the left ventricle was isolated, minced, and filtered for single-cell isolation. Left ventricular cardiomyocytes were equilibrated with Tyrode's solution containing 1.8 mM $CaCl_2$ for functional analysis as previously described[100].

Human coronary artery endothelial cells (HCAECs). Human Coronary Artery Endothelial Cells (HCAECs) were purchased from Lonza. HCAECs were seeded at a density of 80,000–100,000 cells per well on 12-well plates using EGM-2 MV Microvascular Endothelial Growth Medium (Lonza) supplemented with 10% fetal bovine serum (Gibco). Before each experiment, cells were placed in the EBM-2 medium with 1% fetal bovine serum (FBS) for 16 h (serum starvation). Following serum starvation, non-adherent cells and debris were aspirated and

HCAECs were washed with phosphate-buffered saline (PBS). PAGln was dissolved in EBM-2 media with 1% FBS at 20 and 100 µM concentrations for treatment.

Method details

Transthoracic echocardiography. Two-dimensional (2D) echocardiography was performed on day 20, 9 h after the second binge or on day 20 in the FMT study, or during peak exposure to PAGln in a subset of mice in each study. In the BoCA study, pair-fed control ($n = 10$), alcohol control ($n = 11$), and alcohol + probiotics ($n = 10$); in the FMT study, pair-fed FMT ($n = 7$), alcohol FMT ($n = 8$). A Vevo 2100 ultrasound system (Fujifilm VisualSonics, Toronto, Canada) was used to acquire images for analysis of cardiac structure and function. Anesthesia was induced with isoflurane (2–3%) supplemented with 100% oxygen. Once anesthetized, 2D TTE was performed under isoflurane (1%) to determine cardiac structure and function in a blinded manner.

Invasive hemodynamics. Invasive hemodynamics was performed on a subset of mice in each study as previously described[101]. The BoCA study, consisted of pair-fed controls ($n = 11$), alcohol controls ($n = 11$), and alcohol + probiotics ($n = 10$). The FMT study consisted of pair-fed FMT ($n = 11$) and alcohol FMT ($n = 12$). Animals were anesthetized with 2–3% isoflurane supplemented with 100% oxygen and maintained on 0.5–0.75% isoflurane supplemented with 100% oxygen for the measurement of hemodynamics. A 1.2F solid-state pressure catheter was used to collect invasive hemodynamics in tandem transonic SP100 Scisense Pressure Measurement System (Transonic, NY, USA) and LabChart, Version 2.0 acquisition/analysis software (ADInstruments, CO, USA). The right common carotid artery was isolated and the catheter was introduced retrograde into the aortic root. Systemic blood pressure was recorded for at least 30 s, then the catheter was advanced into the left ventricle through the aortic valve. Again, a 30 s recording was acquired for assessment of left ventricular hemodynamics. An average of three cardiac cycles was used to provide a mean data point for each index per animal.

Metagenomic 16S rRNA sequencing and analysis. Cecal content was collected from mice in all treatment groups in BoCA study ($n = 12$ per group, per study). DNA extraction from cecal bacteria was performed using the QIAamp® Fast DNA Stool Mini Kit (Qiagen, Hilden, Germany) following the manufacturer's protocol with slight modifications. To increase bacterial DNA yield, bead beating was implemented. 16S rRNA gene libraries were prepared per mouse per group and sequenced by the LSUHSC, School of Medicine Microbial Genomics Resource Group.

To generate the library, PCRs were performed to amplify the V4 region of the16S rRNA gene, which incorporates targeted primers and the Illumina overhang adapter. After quantification and qualification, samples were pooled in equimolar amount and pair-end 2 × 250 bp sequencing was performed on Illumina MiSeq platform (Illumina, San Diego, CA, US) using a 500 cycle V2 sequencing kit. 16S rRNA gene sequencing raw data (accession number PRJNA851080) were deposited in the National Center for Biotechnology Information Sequence Read Archive. The sequencing data was processed by QIIME2 software pipeline v2021.11[102]. In general, trimmed sequences were merged and filtered. Pair-end sequences were then clustered into operational taxonomic units (OTUs) using open reference OTU picking performed against Greengenes bacterial 16S rRNA database (13_8 release) with 97% similarity threshold. Alpha-diversity (diversity within sample community species richness) was determined with ten iterations at a maximal sequence depth where all samples could be included. Beta-diversity (between sample communities dissimilarity) was calculated using weighted and unweighted UniFrac distances[103]. To explore the differentiated taxa, one-way ANOVA and LefSe analyses were performed[104].

Plasma sample preparation. Plasma was collected during the terminal procedure via an inferior vena cava stick with a 27-gauge needle and 1 cc syringe. After collection, blood was quickly transferred to an EDTA-coated collection tube and placed on ice prior to centrifugation. Plasma was separated through centrifugation (4000 *g*, 10 min, 4 °C). A small aliquot was acidified for LC-MS/MS analysis of microbial-derived metabolites. The remaining plasma was then aliquoted into several cryotubes and flash-frozen in liquid N_2. Samples were stored at −80 °C for future biochemical and molecular analysis.

HPLC quantification of nitrite levels. In a subset of mice per group per study, plasma nitrite levels were measured using Eicom's ENO-30 (Amuza Inc, CA, USA), which is a Nox analyzer using high-pressure liquid chromatography methodology to measure nitrite in biological samples as previously described[105]. The BoCA study contained pair-fed ($n = 18$), alcohol controls ($n = 19$), and alcohol + probiotics ($n = 26$); for the FMT study, pair-fed FMT ($n = 9$) and alcohol FMT ($n = 12$), for the PAGln study, vehicle ($n = 5$–10) and PAGln ($n = 5$–10). Plasma (50 µl) was thawed on ice and supplemented with 100% methanol (1:1 ratio). Tissue samples were then centrifuged at (10,000 × *g*, 20 min, 4 °C) to separate out any precipitation. The supernatant was collected and nitrite measurements were performed. The area under the peak was calculated and plotted against a standard curve produced by varying concentrations (5–0.78125 µM) of sodium nitrite.

Circulating Levels of 8-Isoprostane. Plasma 8-isoprostane levels were measured by enzyme-linked immunosorbent assay (ELISA) kit (Cayman Chemical, MI, USA), as per manufacturer protocol. The measurement was performed in the following number of animals per group per study, at the terminal timepoint: pair-fed controls ($n = 19$), alcohol controls ($n = 20$), alcohol + probiotics ($n = 25$); pair-fed FMT ($n = 10$), alcohol FMT ($n = 12$); vehicle ($n = 10$) and PAGln ($n = 10$).

Inflammatory cytokine array. Plasma samples from the BoCA study ($n = 4$ in each group) were used to determine the circulating levels of 62 cytokines using an antibody-pair-based membrane array (Abcam, Cambridge, UK). Targets included Axl, BLC, CD30 L, CD30, CD40, CRG-2, CTACK, CXCL16, Eotaxin, Eotaxin-2, Fas Ligand, Fractalkine, GCSF, GM-CSF, IFN-gamma, IGFBP-3, IGFBP-5, IGFBP-6, IL-1beta, IL-10, IL-12 p40/p70, IL-12 p70, IL-13, IL-17, IL-1alpha, IL-2, IL-3, IL-3 Rbeta, IL-4, IL-5, IL-6, IL-9, KC/CXCL1, Leptin/OB, Leptin R, LIX, L-Selectin, Lymphotactin, MCP1, MCP-5, M-CSF, MIG, MIP-1 alpha, MIP-1 gamma, MIP-2, MIP-3beta, MIP-3alpha, PF-4, P-Selectin, RANTES, SCF, SDF-1alpha, sTNF RI, sTNF RII, TARC, TCA-3, TECK, TIMP-1, TNFalpha, Thrombopoietin, VCAM-1, and VEGF-A. The experiment was run per manufacturer protocol. Briefly, membranes were incubated with plasma samples at 1:5-1:8 dilution overnight at 4 °C on plate shaker. Membranes were then washed using LiCor wash buffer ® and probed with fluorescent secondary. Imaging of the membranes was performed with a LiCor Odyssey CLx® and Image Studio software version 5.2. Each membrane was imaged separately under the following parameters: Channel 800λ with a scan resolution of 84 µm and a scan quality of medium. Analysis normalized the positive fluorescent markers on each membrane to that of the membrane negative controls. Subsequently, the AF and AF + P ($n = 7$, each) expression of each cytokine was normalized to the expression of each marker in the PF group ($n = 7$). Data are plotted as the fold change from PF group indicated by heatmap.

Aortic vascular reactivity. Ex vivo vascular reactivity experiments were performed in isolated aortic rings as previously described[106]. In the BoCA Study, aortic rings were isolated and studied in pair-fed controls ($n = 8$), alcohol controls ($n = 7$), and alcohol + probiotics ($n = 8$) after 20 days of study; in the FMT study, pair-fed FMT ($n = 7$), and alcohol FMT ($n = 8$). Finally, in the PAGln study, vehicle and PAGln groups ($n = 8$, each) after 20 days of study. Immediately upon

euthanasia, thoracic aorta was dissected and cleaned of all debris in ice-cold Krebs buffer. Arteries were cut into 3 mm length rings and submerged in organ bath chambers with 37 °C Krebs buffer for isometric tension experiments. Rings were placed under an initial tension of 1.0 g of force for 120 min to obtain a stable steady state on the tissue organ bath system (Radnoti, Covina, CA). Arteries were then initially subjected to 40 mM and next 100 mM potassium chloride. Following incubation with potassium chloride, arteries were washed and aortic rings were pre-contracted with 1 μM phenylephrine. Once peak constriction was achieved, rings were subjected to varying concentrations of sodium acetylcholine (Ach; 10^{-9}–10^{-5} M) or sodium nitroprusside (SNP; 10^{-10}–10^{-5} M).

LC-MS/MS quantification of gut microbial-derived metabolites. For human serum metabolite analysis, sample preparation and analysis were conducted at Metabolon (Durham, NC), as previously detailed[13,95,96]. Metabolites were identified by comparing ion features in the experimental samples to a reference library of chemical standards, which included retention time, molecular weight (*m/z*), preferred adducts, in-source fragments, and associated MS spectra[13].

Targeted metabolite analyses on a wide range of gut microbial aromatic amino acid-derived metabolites and TMAO-related metabolites were previously conducted to investigate their clinical associations with incident of major adverse cardiac event (MACE) risks across multiple cohorts (over 4000 human plasma samples)[107]. In the present study an aliquot of acidified murine plasma (100 μl) (1 N HCL with a dilution of sample not greater than 10%) and frozen tissue specimens (cardiac, liver, and kidney) from a subset of animals in the BoCA study (pair-fed [$n = 5$–7], alcohol ± probiotics [$n = 13$, each]), FMT study (PF-FMT [$n = 10$], AF-FMT [$n = 6$–7]) and PAGln study (Vehicle [$n = 3$], PAGln [$n = 5$–6]) were processed for LC-MS/MS quantification of targeted gut microbial-derived metabolites.

Briefly, different concentrations of various standards were prepared to cover the ranges of each metabolite quantified from over 4000 sequential human plasma samples. These standards were then mixed with a consistent internal standard mix to create calibration curves. The resulting standard curves demonstrated excellent linearity over a wide concentration range (Supplementary Fig. 3, all $r^2 > 0.99$ except $r^2 = 0.960$ for phenylacetic acid and $r^2 = 0.989$ for 4-OH phenyllactic acid). The detection limit for each metabolite using our LC/MS system was 0.01 μM. Quality control plasma samples, included every 28 sequential plasma samples, showed that all monitored metabolites had a coefficient of variation (CV) of less than 15% (Supplementary Fig. 8). The quantification of plasma aromatic amino acid metabolites, PAA, PAGly, PAGln, and TMAO related metabolites was conducted by combining 10 μl of plasma with 40 μl of cold methanol containing individual isotope-labeled internal standard mix, followed by ultracentrifugation and LC/MS/MS analysis, following established protocols[108]. Tissues subjected to repeated freeze-thaw cycles were homogenized at 20 μL/mg tissue of cold water in a 2 ml Eppendorf tube using a metal bead beater operating at 30 Hz for 5 min in a TissueLyser III (Qiagen). Following centrifugation at 10,000 *g* for 10 min at 4 °C, the supernatant was collected for the above metabolite quantification, following the same procedure as for plasma samples.

Histological processing and quantification. Colon and liver tissue were fixed in neutral buffered formalin, embedded in paraffin, and 4-μm-thick histological cross-sections were stained with hematoxylin and eosin (H&E). Immunohistochemistry for colon tight junction proteins (ZO-1, claudin-1, and occludins) was performed. Briefly, after antigen retrieval using 10 mmol/L citrate buffer (pH 6.0; Abcam), colon sections were blocked with 10% goat serum for 1 h at room temperature. Then sections were incubated with antibodies: rabbit anti-ZO-1 (1:500; Invitrogen), or rabbit anti-claudin-1 (1:200; Invitrogen), or rabbit anti-Occludin (1:1000, Invitrogen, Carlsbad, CA) overnight at 4 °C, followed by incubation with secondary antibody Goat anti-rabbit IgG Alexa Fluor 488 (1:400; Thermo Fisher) for 1 h at room temperature in the dark. Sections were mounted with ProLong Gold Anti-fade Reagent with DAPI (Invitrogen). To quantify the mean florescence intensity (MFI) in each colon section in ImageJ software (NIH, Bethesda, MD), three cross sections for each mouse were analyzed with an optical microscope (magnification, 20×).

StageBio: Mouse spleen and lung tissues were also used as controls. Primary Antibodies VCAM1 (Abcam, ab271899), as well as matching Rabbit IgG isotope (Abcam, ab37415) were the same as used for immunofluorescent staining. Study tissues were stained using the following staining protocol for individual, chromogenic detection of VCAM1:

Immunohistochemical staining was performed by an automated procedure using the Biocare Medical IntelliPATH FLX. Slides with sections of heart and liver tissue were deparaffinized and rehydrated from xylene to water using a decreasing gradient of alcohol. Next, slides were coated in Diva Decloaker (Biocare Medical, DV2004) and placed in the Decloaking Chamber for 25 min at 95 °C. After cooling for 15 min, slides were loaded onto the IntelliPATH FLX and incubated with Peroxidazed 1 (Biocare Medical, PX968) for 5 min, followed by Background Punisher (Biocare Medical, BP974) for 10 min. Next, slides were coated with the Primary Antibody or matching isotype, each diluted with Monet Blue Diluent (Biocare Medical, PD901) at a working concentration of 1 μg/mL for 60 min. Rabbit on Rodent HRP Polymer (Biocare Medical, RMR622) was then added for 30 min, followed by Betazoid DAB (Biocare Medical, BDB2004) for 5 min. Lastly, slides were counterstained with Mayer's Hematoxylin (Electron Microscopy Sciences, 26609-03), dehydrated through an ascending alcohol gradient and placed in xylene, and cover slipped.

All resulting slides were digitally scanned using the Hamamatsu Nano Zoomer S60 and provided to the Study Pathologist, Sureshkumar Muthupalani, BVSc, MVSc, PhD, DACVP, to review staining success and quality. Upon review, the VCAM1 assays were considered successful and of good quality, with intermediate-to-strong intensity specific staining of vasculature in both control lung and spleen, with additional VCAM1-specific strong intensity staining of splenic red pulp hematopoietic cells. Non-specific background staining was minimal-to-absent with isotype controls in control lung and spleen tissues for VCAM1 assay. In the study tissues, specific VCAM1 intermediate-intensity vascular endothelial staining was identified in the liver and with low-intensity positive endothelial staining in the heart. Minimal-to-mild variable intensity non-specific background staining was identified within heart (cardiomyocytes) and liver (hepatocytes). A Keyence® BZ-X810 microscope was used to acquire serial images on stained slides at 20× magnification. Quantification of the amount of VCAM-1 staining was performed with ImageJ software and plotted at the positive stain over the total tissue area.

Intestinal and hepatic biochemical analysis (iFABP, AST, ALT). Plasma levels of aspartate aminotransferase (Abcam, Cambridge, MA) and alanine aminotransferase (Cloud-Clone, Katy, TX) were determined with commercial kits. Intestinal fatty acid binding protein (iFABP) in plasma was detected with ELISA kit (Boster Bio, Pleasanton, CA, USA). Blood alcohol level was determined with EnzyChrom Ethanol Assay Kit (BioAssay Systems, Hayward, CA, USA).

Quantification of fecal IgA. Collected 50 mg fecal pellets were homogenized in 1 mL PBS with protease inhibitor cocktail (Roch) and placed on ice for 30 min. To collect the supernatant, homogenate was centrifuged at 12,000 *g* × 5 min at 4 °C. Total fecal IgA was measured by sandwich ELISA. In brief, ELISA plates (VWR) were coated with 100 μL 250 ng/mL goat anti-mouse IgA (ThermoFisher) capture antibody overnight at 4 °C. Plates were washed and blocked with 0.1% BSA in PBST for 15 min at room temperature. Diluted samples and standard-

mouse IgA (SouthernBiotech) were added and incubated overnight at 4 °C. Captured IgA was detected by biotinylated goat anti-mouse (SouthernBiotech). Then neutralite avidin- horseradish peroxidase (HRP) (SouthernBiotech) was added and incubated at room temperature for 30 min. Color was then developed by TMB (Surmodics) and quenched by 1 M H_2SO_4. Colorimetric reaction was measured at OD = 450 nm by a Microplate Reader (BioTek Instruments, Inc. Winooski, Vt).

Quantitative real-time PCR. Liver and jejunum total RNA was extracted using TRIzol reagent (Invitrogen) following the instructions, prior to cDNA synthesis. Followed by cDNA synthesis using the High-Capacity cDNA Reverse Transcription Kit (Bio-Rad, Hercules, CA). Real-time quantitative PCR was performed with the Stratagene Mx3000P quantitative PCR system (Agilent Technologies, Santa Clara, CA). Primers' sequences were listed in Key Resource Table. Relative expression was calculated by normalization with β-actin housekeeping gene.

For in vitro experiments using HCAECs, total RNA was extracted using TRIzol reagent (Invitrogen) following the manufacturer's instructions. cDNA synthesis was performed using the Verso cDNA Synthesis Kit (Thermo Scientific). The real-time quantitative PCR reactions were performed with the BioRad CFX Opus Real-Time PCR Systems machine in 96-well reaction plates. Reaction volumes were 20 µl, containing 9 µl cDNA, 10 µM of each pair of primers and SYBR Green Supermix (Bio-Rad). All reactions were run in duplicates. Relative gene expression was calculated by normalization with *18S* housekeeping gene.

Flow cytometry. Bacteria cell death and injury were detected as reported previously[104]. Fecal samples were diluted 1:10 in sterile PBS. The same centrifugation steps were taken to obtain clean cells. Cell pellets were dissolved in PBS and assessed with two fluorescent stains: propidium iodide (Pi) and bis-(1,3-dibutylbarbituric acid) trimethine oxonol [DiBAC4(3)], allowing the observation of cells with loss of membrane integrity and membrane polarity and with distinct nucleic acid content, respectively. Cells were stained in the dark under anaerobic conditions after testing sample preparation and staining conditions. Samples were then washed 2 times with 1 mL staining buffer before being run through BD FACSCanto II flow cytometry (BD Bioscience, Franklin Lakes, New Jersey, USA). Flow data was analyzed FlowJo software (BD).

Cardiomyocyte fractional shortening, calcium transients. Adult mouse left ventricular cardiomyocytes (LVCMs) were loaded with 0.5 µM Fura2-AM and placed on the stage of an inverted microscope in a chamber containing normal physiological Tyrode's solution (150 mM NaCl, 5.4 mM KCl, 1.2 mM $MgCl_2$, 10 mM glucose, 2 mM Na-pyruvate, 1.8 mM $CaCl_2$, and 5 mM HEPES, pH 7.35)[100]. Cardiomyocytes were paced with an IonOptix Myocyte Calcium and Contractility system at 0.5 Hz continuously. Fractional shortening was measured by sarcomere length detection and changes in intracellular calcium levels were monitored using Fura2 dual excitation (340/380 nm) single emission (510 nm) ratiometric imaging. Contractility and calcium transients were measured at baseline and with exposure to varying concentrations of PAGln (2, 5, 10, 50 200 µM). LVCMs were also exposed to 10 nM isoproterenol ± 1µM carvedilol (pretreatment for 10 min). In a second set of experiments, isolated cardiomyocytes underwent the same field stimulation with 2 µM PAGln ± 1µM carvedilol (pretreatment for 10 min); 10 nM isoproterenol was used as a positive control for β-adrenergic agonism ± 1µM carvedilol (pretreatment for 10 min). Data was processed using IonWizard analysis software.

Protein expression by western blotting. Isolated adult mouse left ventricular cardiomyocytes were collected and exposed to the above varying conditions. Cells were pelleted and extracts were generated using RIPA buffer. Protein lysate concentrations were determined by BCA assay. Standard Western blotting protocol was performed using HRP-conjugated secondary antibodies for detection and blots were imaged and quantified using a ChemiDoc MP Imaging System.

Liver tissue from the PAGln i.p. study was homogenized in RIPA buffer containing protease and phosphatase inhibitors. Homogenized material was centrifuged (15,000 *g*/15 min/4 °C) and supernatant collected. Protein lysate concentrations were determined by BCA assay. Standard Western blotting protocol was performed using fluorescent secondary antibody Goat anti-Rabbit IRDye680 for detection. Blots were imaged using LI-COR Imaging System and densitometry was performed in ImageJ.

HCAEC cells were cultured per manufacturer's protocol to ~80–90% confluency in proprietary media and exposed to PAGln (100 µM) or lipopolysaccharides (LPS) (100 ng/ml) for varying periods of time (1, 4, 6, 8, 12, 24, and 48 h). Cells were collected in RIPA buffer supplemented with protease and phosphatase inhibitors and flash frozen. Protein lysate was derived from sonication and centrifugation at 4 °C/15,000 *g*/15 min. Protein concentrations were determined using BCA assay. Standard Western blotting protocol was performed using HRP-conjugated secondary antibodies for detection. Image quantification was performed using Bio-Rad Image Lab System.

Reactive oxygen species (ROS) assay. HCAECs were plated to 80–90% confluency in six well dishes coated in gelatin. Cells were incubated with CellROX™ green reagent (ThermoFisher Scientific) for 30-min prior to the addition of conditioned media. Treatment groups included 1000 ng/ml LPS (positive control), standard media (vehicle) or 100 µM PAGln. Brightfield, phase contrast and fluorescent images were acquired every 30-min for 12-h using BioTek Cytation C10® Imaginer at 20× magnification. GFP^+ area was plotted against total image area across time as a percentage.

Wound healing scratch assay. HCAECs were plated to 80–90% confluency in six-well dishes coated in gelatin. Treatments include HCAEC culture media (vehicle) or HCAEC culture media supplemented with 100 µM PAGln ($n = 6$ wells each). For the 24-h incubation group, cells had no prior exposure to PAGln before initiation of the scratch assay. In the 48-h preincubation group, cells had 48-h PAGln exposure before starting the scratch assay. A scratch was performed using 1000 µl pipette tip. Once completed, the cells were washed with media one time, then 2 mls of vehicle or conditioned media were added to the wells. Plates were loaded into BioTek Cytation C10® imaginer for phase contrast and fluorescent imaging at 4× magnification with a 3 × 2 stitching of images every hour for 24-h. Analysis was performed by subtracting the cellular area from total area to provide a wound area, which is plotted as a percent change from initial wound area across time. Linear regression analysis was performed.

Quantification and statistical analysis

All data are presented as box and whisker plots with individual measurement dot plots unless otherwise specified. Data were tested for a Gaussian distribution using the Shapiro-Wilk normality test. To determine outliers the ROUT method was used and is based on the False Discovery Rate (FDR), specifying $Q = 1\%$, which is the maximum desired FDR. When there are no outliers (and the distribution is entirely Gaussian), Q is very similar to alpha. Assuming all data come from a Gaussian distribution, Q is the chance of (falsely) identifying one or more outliers. If the data were parametric, a student's *T*-test or ordinary one-way ANOVA with Holm-Šídák multiple comparisons test with a single pooled variance was performed. Nonparametric data underwent the Mann-Whitney Test or Kruskal-Wallis Test with Dunn's multiple comparisons test unless otherwise specified. Significance was determined by a p-value < 0.05. Exact p-values are provided. Graphs production and statistical analysis were performed in GraphPad Prism v10.1.1.

Resource availability

Further information for key resources can be found in Supplementary Table 6 and upon requests for resources and reagents should be directed to and will be fulfilled by the Lead Contact, Thomas E. Sharp, III (tesharp@usf.edu).

Reporting summary

Further information on research design is available in the Nature Portfolio Reporting Summary linked to this article.

Data availability

The data that support the findings of this study are provided in the Supplementary Information/Source Data file. The 16S rRNA gene sequencing raw data used in this study are available in the National Center for Biotechnology Information Sequence Read Archive under accession number PRJNA851080. Any additional information required to reanalyze the data reported or support the findings in this paper is available from the corresponding author (T.E.S.) upon reasonable request. Source data are provided with this paper.

References

1. Piano, M. R. Alcohol's effects on the cardiovascular system. *Alcohol Res.* **38**, 219–241 (2017).
2. Biddinger, K. J. et al. Association of habitual alcohol intake with risk of cardiovascular disease. *JAMA Netw. Open* **5**, e223849 (2022).
3. Whitman, I. R. et al. Alcohol abuse and cardiac disease. *J. Am. Coll. Cardiol.* **69**, 13–24 (2017).
4. Matyas, C. et al. Chronic plus binge ethanol feeding induces myocardial oxidative stress, mitochondrial and cardiovascular dysfunction, and steatosis. *Am. J. Physiol. Heart Circ. Physiol.* **310**, H1658–H1670 (2016).
5. Singal, A. K. & Mathurin, P. Diagnosis and treatment of alcohol-associated liver disease: a review. *JAMA* **326**, 165–176 (2021).
6. Grander, C. et al. Recovery of ethanol-induced Akkermansia muciniphila depletion ameliorates alcoholic liver disease. *Gut* **67**, 891–901 (2018).
7. Tang, W. W. et al. Gut microbiota-dependent trimethylamine N-oxide (TMAO) pathway contributes to both development of renal insufficiency and mortality risk in chronic kidney disease. *Circ. Res.* **116**, 448–455 (2015).
8. Helsley, R. N. et al. Gut microbial trimethylamine is elevated in alcohol-associated hepatitis and contributes to ethanol-induced liver injury in mice. *eLife* **11**, e76554 (2022).
9. Nemet, I. et al. Atlas of gut microbe-derived products from aromatic amino acids and risk of cardiovascular morbidity and mortality. *Eur. Heart J.* **44**, 3085–3096 (2023).
10. Poesen, R. et al. Microbiota-derived phenylacetylglutamine associates with overall mortality and cardiovascular disease in patients with CKD. *J. Am. Soc. Nephrol.* **27**, 3479–3487 (2016).
11. Nemet, I. et al. A cardiovascular disease-linked gut microbial metabolite acts via adrenergic receptors. *Cell* **180**, 862–877.e822 (2020).
12. Fu, H., Kong, B., Zhu, J., Huang, H. & Shuai, W. Phenylacetylglutamine increases the susceptibility of ventricular arrhythmias in heart failure mice by exacerbated activation of the TLR4/AKT/mTOR signaling pathway. *Int. Immunopharmacol.* **116**, 109795 (2023).
13. Liu, D. et al. Serum metabolomic analysis reveals several novel metabolites in association with excessive alcohol use—an exploratory study. *Transl. Res.* **240**, 87–98 (2022).
14. Paloczi, J. et al. Alcohol binge-induced cardiovascular dysfunction involves endocannabinoid-CB1-R signaling. *JACC Basic Transl. Sci.* **4**, 625–637 (2019).
15. Llopis, M. et al. Intestinal microbiota contributes to individual susceptibility to alcoholic liver disease. *Gut* **65**, 830–839 (2016).
16. Zhang, Y. et al. Bifidobacterium animalis A12 and *Lactobacillus salivarius* M18-6 alleviate alcohol injury by keap1-Nrf2 pathway and thioredoxin system. *Foods* **12**, 439, (2023).
17. Rachmilewitz, D. et al. Toll-like receptor 9 signaling mediates the anti-inflammatory effects of probiotics in murine experimental colitis. *Gastroenterology* **126**, 520–528 (2004).
18. Kupari, M., Koskinen, P., Suokas, A. & Ventilä, M. Left ventricular filling impairment in asymptomatic chronic alcoholics. *Am. J. Cardiol.* **66**, 1473–1477 (1990).
19. Agerholm-Larsen, L. et al. Effect of 8 week intake of probiotic milk products on risk factors for cardiovascular diseases. *Eur. J. Clin. Nutr.* **54**, 288–297 (2000).
20. Paulus, W. J. et al. How to diagnose diastolic heart failure: a consensus statement on the diagnosis of heart failure with normal left ventricular ejection fraction by the Heart Failure and Echocardiography Associations of the European Society of Cardiology. *Eur. Heart J.* **28**, 2539–2550 (2007).
21. Sharp, T. E. et al. Renal denervation prevents heart failure progression via inhibition of the renin-angiotensin system. *J. Am. Coll. Cardiol.* **72**, 2609–2621 (2018).
22. Kleinbongard, P. et al. Plasma nitrite concentrations reflect the degree of endothelial dysfunction in humans. *Free Radic. Biol. Med.* **40**, 295–302 (2006).
23. Mutlu, E. A. et al. Colonic microbiome is altered in alcoholism. *Am. J. Physiol.-Gastrointest. Liver Physiol.* **302**, G966–G978 (2012).
24. Leclercq, S. et al. Intestinal permeability, gut-bacterial dysbiosis, and behavioral markers of alcohol-dependence severity. *Proc. Natl Acad. Sci.* **111**, E4485–E4493 (2014).
25. Manor, O. et al. Health and disease markers correlate with gut microbiome composition across thousands of people. *Nat. Commun.* **11**, 5206 (2020).
26. Rizzatti, G., Lopetuso, L. R., Gibiino, G., Binda, C. & Gasbarrini, A. Proteobacteria: a common factor in human diseases. *Biomed. Res. Int.* **2017**, 9351507 (2017).
27. Meena, A. S. et al. TRPV6 channel mediates alcohol-induced gut barrier dysfunction and systemic response. *Cell Rep.* **39**, 110937 (2022).
28. Thevaranjan, N. et al. Age-associated microbial dysbiosis promotes intestinal permeability, systemic inflammation, and macrophage dysfunction. *Cell Host Microbe* **21**, 455–466. e454 (2017).
29. Zeisel, M. B., Dhawan, P. & Baumert, T. F. Tight junction proteins in gastrointestinal and liver disease. *Gut* **68**, 547–561 (2019).
30. Lee, Y. K. & Mazmanian, S. K. Has the microbiota played a critical role in the evolution of the adaptive immune system? *Science* **330**, 1768–1773 (2010).
31. Cullen, T. et al. Antimicrobial peptide resistance mediates resilience of prominent gut commensals during inflammation. *Science* **347**, 170–175 (2015).
32. Ganz, T. et al. Defensins. Natural peptide antibiotics of human neutrophils. *J. Clin. Investig.* **76**, 1427–1435 (1985).
33. Kramer, B. & Muranyi, P. Effect of pulsed light on structural and physiological properties of *Listeria innocua* and *Escherichia coli*. *J. Appl. Microbiol.* **116**, 596–611 (2014).
34. Brown, J. M. & Hazen, S. L. The gut microbial endocrine organ: bacterially derived signals driving cardiometabolic diseases. *Annu. Rev. Med.* **66**, 343–359 (2015).
35. Zhu, Y. et al. Two distinct gut microbial pathways contribute to meta-organismal production of phenylacetylglutamine with links to cardiovascular disease. *Cell Host Microbe* **31**, 18–32.e19 (2023).
36. Tamburini, F. B. et al. Precision identification of diverse bloodstream pathogens in the gut microbiome. *Nat. Med.* **24**, 1809–1814 (2018).
37. Rastogi, S. & Singh, A. Gut microbiome and human health: exploring how the probiotic genus Lactobacillus modulate immune responses. *Front. Pharm.* **13**, 1042189 (2022).

38. Skye, S. M. et al. Microbial transplantation with human gut commensals containing CutC is sufficient to transmit enhanced platelet reactivity and thrombosis potential. *Circ. Res.* **123**, 1164–1176 (2018).
39. Xia, H. et al. Endothelial cell cystathionine γ-lyase expression level modulates exercise capacity, vascular function, and myocardial ischemia reperfusion injury. *J. Am. Heart Assoc.* **9**, e017544 (2020).
40. Chu, G. et al. A single site (Ser16) phosphorylation in phospholamban is sufficient in mediating its maximal cardiac responses to beta-agonists. *J. Biol. Chem.* **275**, 38938–38943 (2000).
41. Yoshikawa, T. et al. Cardiac adrenergic receptor effects of carvedilol. *Eur. Heart J.* **17 Suppl B**, 8–16 (1996).
42. Aslanian, A. M. & Charo, I. F. Targeted disruption of the scavenger receptor and chemokine CXCL16 accelerates atherosclerosis. *Circulation* **114**, 583–590 (2006).
43. Chen, G. et al. CXCL16 recruits bone marrow-derived fibroblast precursors in renal fibrosis. *J. Am. Soc. Nephrol.* **22**, 1876–1886 (2011).
44. Wehr, A. et al. Chemokine receptor CXCR6-dependent hepatic NK T Cell accumulation promotes inflammation and liver fibrosis. *J. Immunol.* **190**, 5226–5236 (2013).
45. Fleming, I., Fisslthaler, B., Dimmeler, S., Kemp, B. E. & Busse, R. Phosphorylation of Thr(495) regulates Ca(2+)/calmodulin-dependent endothelial nitric oxide synthase activity. *Circ. Res.* **88**, E68–E75 (2001).
46. Michell, B. J. et al. Coordinated control of endothelial nitric-oxide synthase phosphorylation by protein kinase C and the cAMP-dependent Protein Kinase*. *J. Biol. Chem.* **276**, 17625–17628 (2001).
47. Blankenberg, S., Barbaux, S. & Tiret, L. Adhesion molecules and atherosclerosis. *Atherosclerosis* **170**, 191–203 (2003).
48. Cines, D. B. et al. Endothelial cells in physiology and in the pathophysiology of vascular disorders. *Blood* **91**, 3527–3561 (1998).
49. Wu, M. D. K. K. & Thiagarajan, M. D. P. Role of endothelium in thrombosis and hemostasis. *Annu. Rev. Med.* **47**, 315–331 (1996).
50. Chavakis, E. & Dimmeler, S. Regulation of endothelial cell survival and apoptosis during angiogenesis. *Arterioscler. Thromb. Vasc. Biol.* **22**, 887–893 (2002).
51. Dimmeler, S. & Zeiher, A. M. Endothelial cell apoptosis in angiogenesis and vessel regression. *Circ. Res.* **87**, 434–439 (2000).
52. McGovern, P. E. et al. Fermented beverages of pre- and proto-historic China. *Proc. Natl. Acad. Sci.* **101**, 17593–17598 (2004).
53. Thompson, R. C. et al. Atherosclerosis across 4000 years of human history: the Horus study of four ancient populations. *Lancet* **381**, 1211–1222 (2013).
54. Ronksley, P. E., Brien, S. E., Turner, B. J., Mukamal, K. J. & Ghali, W. A. Association of alcohol consumption with selected cardiovascular disease outcomes: a systematic review and meta-analysis. *BMJ* **342**, d671 (2011).
55. Baum-Baicker, C. The health benefits of moderate alcohol consumption: a review of the literature. *Drug Alcohol Depend.* **15**, 207–227 (1985).
56. Ames, N. J. et al. Longitudinal gut microbiome changes in alcohol use disorder are influenced by abstinence and drinking quantity. *Gut Microbes* **11**, 1608–1631 (2020).
57. Lindenbaum, J. & Lieber, C. S. Hematologic effects of alcohol in man in the absence of nutritional deficiency. *N. Engl. J. Med.* **281**, 333–338 (1969).
58. Fang, C. et al. Dysbiosis of gut microbiota and metabolite phenylacetylglutamine in coronary artery disease patients with stent stenosis. *Front. Cardiovasc. Med.* **589**, 832092 (2022).
59. Mrdjen, M. et al. Dysregulated meta-organismal metabolism of aromatic amino acids in alcohol-associated liver disease. *Hepatol. Commun.* **7**, https://doi.org/10.1097/hc9.0000000000000284 (2023).
60. Fernández-Solà, J. Cardiovascular risks and benefits of moderate and heavy alcohol consumption. *Nat. Rev. Cardiol.* **12**, 576–587 (2015).
61. Smirnova, E. et al. Fecal microbiome distinguishes alcohol consumption from alcoholic hepatitis but does not discriminate disease severity. *Hepatology* **72**, 271–286 (2020).
62. Wang, X. et al. Aberrant gut microbiota alters host metabolome and impacts renal failure in humans and rodents. *Gut* **69**, 2131–2142 (2020).
63. Dubinkina, V. B. et al. Links of gut microbiota composition with alcohol dependence syndrome and alcoholic liver disease. *Microbiome* **5**, 141 (2017).
64. Organ, C. L. et al. Nonlethal inhibition of gut microbial trimethylamine N-oxide production improves cardiac function and remodeling in a murine model of heart failure. *J. Am. Heart Assoc.* **9**, e016223 (2020).
65. Zhu, W. et al. Gut microbes impact stroke severity via the trimethylamine N-oxide pathway. *Cell Host Microbe* **29**, 1199–1208.e1195 (2021).
66. Organ, C. L. et al. Nonlethal inhibition of gut microbial trimethylamine N-oxide production improves cardiac function and remodeling in a murine model of heart failure. *J. Am. Heart Assoc.* **9**, e016223 (2020).
67. Fan, Y. & Pedersen, O. Gut microbiota in human metabolic health and disease. *Nat. Rev. Microbiol.* **19**, 55–71 (2021).
68. Romano, K. A. et al. Gut microbiota-generated phenylacetylglutamine and heart failure. *Circ. Heart Fail.* **16**, e009972 (2022).
69. Xiao, L. et al. A catalog of the mouse gut metagenome. *Nat. Biotechnol.* **33**, 1103–1108 (2015).
70. Spudich, J. A. Three perspectives on the molecular basis of hypercontractility caused by hypertrophic cardiomyopathy mutations. *Pflug. Arch.* **471**, 701–717 (2019).
71. Abi-Gerges, N. et al. Multiparametric mechanistic profiling of inotropic drugs in adult human primary cardiomyocytes. *Sci. Rep.* **10**, 7692 (2020).
72. Toepfer, C. N. et al. Myosin sequestration regulates sarcomere function, cardiomyocyte energetics, and metabolism, informing the pathogenesis of hypertrophic cardiomyopathy. *Circulation* **141**, 828–842 (2020).
73. Lerman, A. & Zeiher, A. M. Endothelial function. *Circulation* **111**, 363–368 (2005).
74. Deanfield, J. E., Halcox, J. P. & Rabelink, T. J. Endothelial function and dysfunction. *Circulation* **115**, 1285–1295 (2007).
75. Blake, G. J. & Ridker, P. M. Novel clinical markers of vascular wall inflammation. *Circ. Res.* **89**, 763–771 (2001).
76. Rudic, R. D. et al. Direct evidence for the importance of endothelium-derived nitric oxide in vascular remodeling. *J. Clin. Investig.* **101**, 731–736 (1998).
77. Khan, B. V., Harrison, D. G., Olbrych, M. T., Alexander, R. W. & Medford, R. M. Nitric oxide regulates vascular cell adhesion molecule 1 gene expression and redox-sensitive transcriptional events in human vascular endothelial cells. *Proc. Natl. Acad. Sci.* **93**, 9114–9119 (1996).
78. Pober, J. S. & Sessa, W. C. Evolving functions of endothelial cells in inflammation. *Nat. Rev. Immunol.* **7**, 803–815 (2007).
79. Marchesi, C., Ebrahimian, T., Angulo, O., Paradis, P. & Schiffrin, E. L. Endothelial nitric oxide synthase uncoupling and perivascular adipose oxidative stress and inflammation contribute to vascular dysfunction in a rodent model of metabolic syndrome. *Hypertension* **54**, 1384–1392 (2009).
80. McCabe, T. J., Fulton, D., Roman, L. J. & Sessa, W. C. Enhanced electron flux and reduced calmodulin dissociation may explain

"Calcium-independent" eNOS activation by phosphorylation*. *J. Biol. Chem.* **275**, 6123–6128 (2000).
81. Eroglu, E., Saravi, S. S. S., Sorrentino, A., Steinhorn, B. & Michel, T. Discordance between eNOS phosphorylation and activation revealed by multispectral imaging and chemogenetic methods. *Proc. Natl. Acad. Sci.* **116**, 20210–20217 (2019).
82. Rizwan, S., ReddySekhar, P. & MalikAsrar, B. Reactive oxygen species in inflammation and tissue injury. *Antioxid. Redox Signal.* **20**, 1126–1167 (2014).
83. Landy, E., Carol, H., Ring, A. & Canna, S. Biological and clinical roles of IL-18 in inflammatory diseases. *Nat. Rev. Rheumatol.* **20**, 33–47 (2024).
84. Li, D. & Wu, M. Pattern recognition receptors in health and diseases. *Signal Transduct. Target. Ther.* **6**, 291 (2021).
85. Mostafavi, S. et al. Parsing the interferon transcriptional network and its disease associations. *Cell* **164**, 564–578 (2016).
86. Yasuda, K., Nakanishi, K. & Tsutsui, H. Interleukin-18 in health and disease. *Int. J. Mol. Sci.* **20**, https://doi.org/10.3390/ijms20030649 (2019).
87. Vetrano, A. M. et al. Characterization of the oxidase activity in mammalian catalase. *J. Biol. Chem.* **280**, 35372–35381 (2005).
88. Maines, M. D. & Kappas, A. Cobalt induction of hepatic heme oxygenase; with evidence that cytochrome P-450 is not essential for this enzyme activity. *Proc. Natl. Acad. Sci.* **71**, 4293–4297 (1974).
89. Otterbein, L. E., Soares, M. P., Yamashita, K. & Bach, F. H. Heme oxygenase-1: unleashing the protective properties of heme. *Trends Immunol.* **24**, 449–455 (2003).
90. Yachie, A. et al. Oxidative stress causes enhanced endothelial cell injury in human heme oxygenase-1 deficiency. *J. Clin. Investig.* **103**, 129–135 (1999).
91. Soares, M. et al. Expression of heme oxygenase-1 can determine cardiac xenograft survival. *Nat. Med.* **4**, 1073–1077 (1998).
92. Dröge, W. Free radicals in the physiological control of cell function. *Physiol. Rev.* **82**, 47–95 (2002).
93. Lushchak, V. Oxidative stress concept updated: definitions, classifications, and regulatory pathways implicated. *EXCLI J.* **20**, 956–967 (2021).
94. Bers, D. M. Calcium cycling and signaling in cardiac myocytes. *Annu. Rev. Physiol.* **70**, 23–49 (2008).
95. Yang, Z. et al. Serum metabolomic profiling identifies key metabolic signatures associated with pathogenesis of alcoholic liver disease in humans. *Hepatol. Commun.* **3**, 542–557 (2019).
96. Yang, Z. et al. Unique urine and serum metabolomic signature in patients with excessive alcohol use: an exploratory study. *Alcohol Clin. Exp Res.*, https://doi.org/10.1111/acer.15398 (2024).
97. Bertola, A., Mathews, S., Ki, S. H., Wang, H. & Gao, B. Mouse model of chronic and binge ethanol feeding (the NIAAA model). *Nat. Protoc.* **8**, 627–637 (2013).
98. Samuelson, D. R. et al. Pulmonary immune cell trafficking promotes host defense against alcohol-associated Klebsiella pneumonia. *Commun. Biol.* **4**, 997 (2021).
99. Gu, M. et al. Alcohol-associated intestinal dysbiosis alters mucosal-associated invariant T-cell phenotype and function. *Alcohol Clin. Exp. Res.* **45**, 934–947 (2021).
100. Makarewich, C. A. et al. A caveolae-targeted L-type Ca^{2+} channel antagonist inhibits hypertrophic signaling without reducing cardiac contractility. *Circ. Res.* **110**, 669–674 (2012).
101. Li, Z. et al. Mitochondrial H(2)S regulates BCAA catabolism in heart failure. *Circ. Res.* **131**, 222–235 (2022).
102. Caporaso, J. G. et al. QIIME allows analysis of high-throughput community sequencing data. *Nat. Methods* **7**, 335–336 (2010).
103. Lozupone, C., Lladser, M. E., Knights, D., Stombaugh, J. & Knight, R. UniFrac: an effective distance metric for microbial community comparison. *ISME j.* **5**, 169–172 (2011).
104. Maurice, C. F., Haiser, H. J. & Turnbaugh, P. J. Xenobiotics shape the physiology and gene expression of the active human gut microbiome. *Cell* **152**, 39–50 (2013).
105. Li, Z. et al. Hydrogen sulfide attenuates renin-angiotensin and aldosterone pathological signaling to preserve kidney function and improve exercise tolerance in heart failure. *JACC Basic Transl. Sci.* **3**, 796–809 (2018).
106. Li, Z. et al. Hydrogen sulfide modulates endothelial–mesenchymal transition in heart failure. *Circ. Res.* **132**, 154–166 (2023).
107. Tang, W. H. et al. Intestinal microbial metabolism of phosphatidylcholine and cardiovascular risk. *N. Engl. J. Med.* **368**, 1575–1584 (2013).
108. Wang, Z. et al. Non-lethal inhibition of gut microbial trimethylamine production for the treatment of atherosclerosis. *Cell* **163**, 1585–1595 (2015).

Acknowledgements

This work is supported in part by grants from National Institutes of Health, Department of Defense, and the National Science Foundation to the following authors: (T32 AR065972 and T32 HL069766 to D.W.); (NSF 2018936 and P20 GM103424 to C.M.T.); (R25 HL145817 and U24 DK1132746 to P.Q.); (HL160569 and HL171221 to C.A.M.); (P01 HL147823, R01HL103866 Gut Flora metabolism of dietary carnitine and cardiovascular disease 1HL167831-A1 to S.L.H.); (U01 AA026917, UH3 AA026903, R01AA030312, Department of Veterans Affairs Merit Award 1I01CX000361, I01 BX006202, and Dean's Scholar in Medical Research to SL); (P50 AA024333, RF1 NS133812, R01 DK130227, R01 DK120679, P01 HL147823, and DOD KC2210163 to J.M.B.); (HL146098, HL146514, and HL151398 to D.J.L.); (UH2 AA026226, P60 AA009803, R21 AA027199, U54 GM104940 to D.A.W.); (R01 AA029984 Alcohol induced Gut Dysbiosis and Cardiovascular Disease to T.E.S.). The authors acknowledge StageBio for the histological processing, methods, and staining services. The authors would like to acknowledge the technical expertise of Dr. Meng Luo in performing the methods for metagenomic sequencing at LSUHSC-NO. The authors would also like to acknowledge the original creation of experimental protocols either in part or fully using BioRender®.

Author contributions

Z.L., M.G., and A.Z. performed and analyzed all in vivo studies and gut studies performed in this manuscript. M.G. performed an analysis of 16S rRNA sequencing data and performed intestinal permeability, gut immunity, and bacterial viability experiments, and analysis. A.Z. performed experiments and analysis of alcohol-induced liver damage, imaging, and analysis of vascular histological assessment, and assisted in PAGln study. X.F. performed cardiac liver and renal tissue processing and tandem mass spectrometry for all studies. K.M., M.M., and X.S.L. performed an analysis of circulating gut microbial metabolites from the plasma. Z.Y., J.M., T.T., K.C., M.H., and L.H. all participated in the collection, processing, and analysis of human subject samples. K.G and T.T.V. performed cultured experiments, western blotting, and wound healing assays in HCAECs. D.W. cultured and performed HCAEC experiments and PCR analysis. A.M.G. performed isolated cardiomyocytes in western blot experiments. Z.W. supervised all LC-MS/MS studies on plasma and tissue samples. C.M.T. reviewed the analysis of 16S rRNA sequencing experiments. P.Q. conceptualized and supervised the in vitro HCAEC experiments. C.A.M. performed and analyzed all data pertaining to isolated primary cardiomyocyte studies. S.L.H. conceived and advised on experimental protocols and provide facilities, resources, and personnel to perform LC-MS/MS. S.L. designed, supervised, funded, and conducted clinical acquisition of human serum samples from heavy drinkers and performed metabolomic studies to characterize the circulating metabolome. J.M.B. supervised the analysis of mass spectrometry data for GMM profiling in plasma samples and

advised study design. D.J.L. aided in the design of studies and provided core facilities to measure nitrite. D.A.W. aided in the design and supervised the completion of the BoCA and FMT studies. T.E.S. conceived, designed, supervised, funded, and performed analysis, and drafted and edited the manuscript. All authors contributed, in part, to the drafting or critical review of the manuscript.

Competing interests

Z.W. reports being named as co-inventor on pending and issued patents held by the Cleveland Clinic relating to cardiovascular diagnostics and therapeutics. Z.W. also reports having received royalty payments for inventions or discoveries related to cardiovascular diagnostics or therapeutics from Cleveland Heart Lab, a fully owned subsidiary of Quest Diagnostics and Procter & Gamble. C.M.T. consults for Abbott Laboratories. S.L.H. reports being named as co-inventor on pending and issued patents held by the Cleveland Clinic relating to cardiovascular diagnostics and therapeutics, being a paid consultant for Procter & Gamble and Zehna Therapeutics, having received research funds from Procter & Gamble, Zehna Therapeutics, and Roche Diagnostics, and being eligible to receive royalty payments for inventions or discoveries related to cardiovascular diagnostics or therapeutics from Cleveland HeartLab and Procter & Gamble. All other authors: Z.L., M.G., A.Z., X.F., K.M., M.M., X.S.L., Z.Y., J.M., T.T., K.C., M.H., L.H., K.G., T.T.V., D.W., A.M.G., P.Q., C.A.M., J.M.B., D.J.L., D.A.W., and T.E.S. have no competing interests.

Additional information

Supplementary information The online version contains supplementary material available at https://doi.org/10.1038/s41467-024-55084-2.

Correspondence and requests for materials should be addressed to Thomas E. Sharp III.

Peer review information *Nature Communications* thanks Byoung-Joon Song, and the other, anonymous, reviewers for their contribution to the peer review of this work. A peer review file is available.

[1]Department of Cardiac Surgery, Smidt Heart Institute, Cedars-Sinai Medical Center, Los Angeles, CA, USA. [2]Section of Pulmonary/Critical Care and Allergy/Immunology, Department of Medicine, Louisiana State University Health Science Center, New Orleans, LA, USA. [3]Comprehensive Alcohol Research Center, School of Medicine, Louisiana State University Health Science Center, New Orleans, LA, USA. [4]Department of Cardiovascular & Metabolic Sciences, Lerner Research Institute, Cleveland Clinic, Cleveland, OH, USA. [5]Center for Microbiome and Human Health, Learner Research Institute, Cleveland Clinic, Cleveland, OH, USA. [6]Department of Cancer Biology, Lerner Research Institute, Cleveland Clinic, Cleveland, OH, USA. [7]Northern Ohio Alcohol Center (NOAC), Cleveland Clinic, Cleveland, OH, USA. [8]Division of Gastroenterology and Hepatology, Department of Medicine, Indiana University School of Medicine, Indianapolis, IN, USA. [9]Department of Medical and Molecular Genetics, Indiana University School of Medicine, Indianapolis, IN, USA. [10]Department of Molecular Pharmacology and Physiology, Morsani College of Medicine, University of South Florida, Tampa, FL, USA. [11]Integrative Biology and Physiology, University of California, Los Angeles, CA, USA. [12]The Heart Institute, Division of Molecular Cardiovascular Biology, Cincinnati Children's Hospital Medical Center, Cincinnati, OH, USA. [13]Department of Microbiology, Immunology and Parasitology, Louisiana State University Health Science Center, New Orleans, LA, USA. [14]Department of Pediatrics, University of Cincinnati College of Medicine, Cincinnati, OH, USA. [15]Heart and Vascular and Thoracic Institute, Cleveland Clinic, Cleveland, OH, USA. [16]Department of Biochemistry and Molecular Biology, Indiana University School of Medicine, Indianapolis, IN, USA. [17]Roudebush Veterans Administration Medical Center, Indianapolis, IN, USA. [18]Heart Institute, Morsani College of Medicine, USF Health, University South Florida, Tampa, FL, USA. [19]Present address: International Flavors and Fragrances Health and Bioscience, Shanghai, China. ✉e-mail: tesharp@usf.edu